Highlights

The Atmospheric Radiative Transfer Simulator ARTS, Version 2.6 — Deep Python Integration

Stefan A. Buehler, Richard Larsson, Oliver Lemke, Simon Pfreundschuh, Manfred Brath, Ian Adams, Stuart Fox, Florian E. Roemer, Paulina Czarnecki, Patrick Eriksson

- The radiative transfer simulator ARTS is now deeply integrated with the Python programming language and available as a standard conda Python package
- It allows the simulation of remote sensing observations and energy fluxes throughout the terrestrial and solar spectral range.

The Atmospheric Radiative Transfer Simulator ARTS, Version 2.6 — Deep Python Integration

Stefan A. Buehler[a], Richard Larsson[a], Oliver Lemke[a], Simon Pfreundschuh[b], Manfred Brath[a], Ian Adams[c], Stuart Fox[d], Florian E. Roemer[a], Paulina Czarnecki[e], Patrick Eriksson[b]

[a] *Meteorological Institute, Center for Earth System Research and Sustainability (CEN), University of Hamburg, Hamburg, Germany*
[b] *Department of Space, Earth and Environment, Chalmers University of Technology, Gothenburg, Sweden*
[c] *Mesoscale Atmospheric Processes Laboratory, NASA Goddard Space Flight Center, Greenbelt, Maryland, United States*
[d] *Met Office, FitzRoy Road, Exeter, EX1 3PB, UK*
[e] *Columbia University, New York, New York, United States*

Abstract

The atmospheric radiative transfer simulator ARTS is a software for computing atmospheric absorption, scattering, the transfer of radiation through an atmosphere, and sensor characteristics. It is written in C++ and can simulate remote sensing observations and radiative energy fluxes. The article describes version 2.6 of the software. There are numerous changes compared to the last ARTS publication, the most striking being that the program is now controlled by Python scripts, which is convenient and allows for great flexibility. The article discusses the ARTS history, the theory behind the computations of absorption and radiative transfer, available solvers for atmospheres with scattering, the computation of energy fluxes and heating rates, and the built-in system for inverting remote observations to atmospheric state variables by optimal estimation. ARTS is publicly available, open source, and free of charge.

Keywords: atmospheric radiative transfer simulator; ARTS; absorption; scattering; line-by-line; energy fluxes
PACS: 42.68.Ay, 42.68.Ca, 42.68.Ge, 42.68.Mj

1. Introduction

1.1. Basics

The Atmospheric Radiative Transfer Simulator ARTS is a software, written primarily in C++, for calculating atmospheric absorption and scattering, and for simulating the transfer of radiation through planetary atmospheres. Philosophically, what sets it apart from other such programs is its very wide scope and its flexibility, unmatched by any other software that the authors are aware of.

ARTS can do radiative transfer simulations in 1D, 2D, and 3D spherical atmospheres, spherical geometry being a key feature for simulating limb observations. It is used for simulating remote sensing observations and retrieval, but also to compute radiative fluxes and heating rates as a reference for faster radiation schemes in atmospheric circulation models for climate research and weather forecasting.

The radiative transfer is fully polarised, allowing simulation of up to four Stokes components, which is important for simulating sensors with polarisation capabilities, and even sometimes for correctly simulating simple polarisation sensors observing at frequencies where the radiation is polarised, for example by Zeeman splitting.

ARTS also does analytical or semi-analytical Jacobians (derivatives of the simulated observation with respect to changes in atmospheric state or model parameters), and these can be used in a built-in optimal estimation method (OEM) implementation for atmospheric state retrieval.

A significant part of ARTS deals with the calculation of absorption spectra from line-by-line spectroscopic data catalogues. In line with the overall philosophy, also this part is very flexible, allowing for example calculations with broadening gases other than air, to the extent that broadening parameters are available. This is important for simulating radiation on other planets.

Additionally, other types of absorption can be added, including predefined continua, measured absorption cross-sections, and collision-induced absorption spectra.

For simulations with scattering, a number of different scattering solvers are available, including a native scheme based on lambda-iteration (DOIT), a native Monte-Carlo scheme, and also well-known schemes such as DISORT. There also is a sophisticated system for specifying the single scattering properties that are needed for these simulations.

1.2. History

Historically, ARTS started in 2000 as a collaboration between Patrick Eriksson (Chalmers) and Stefan Buehler (then University of Bremen). The program was open source from the start and many others have made important contributions over the years.

Important early milestones were the addition of water vapor continuum absorption by Thomas Kuhn [1] and the iterative scattering solver by Claudia Emde and Sreerekha T. R. [2, 3]. Eriksson et al. [4] describes the first OEM implementation (in Matlab) and Buehler et al. [5] gives the first ARTS overview.

Cory Davis [6] added a Monte Carlo scattering solver and Christian Melsheimer [7] did a first validation and intercomparison with other radiative transfer models. Buehler et al. [8] describes the first application of ARTS for radiative flux and cooling rate calculations, and Eriksson et al. [9] developed the matrix sensor representation that is still in use today. Buehler et al. [10] developed a method to represent integral radiation quantities by a few representative frequencies, Buehler et al. [11] describes the handling of absorption in lookup tables, and Eriksson et al. [12] is the second ARTS overview paper.

In 2014, Richard Larsson added code to handle Zeeman splitting [13, 14]. This code was revised over the years and Zeeman splitting coefficients were updated for oxygen and other species [15, 16].

For calculations with ice particle scattering, dedicated databases of single scattering data for different particle shapes and sizes were developed for ARTS for both randomly oriented [17] and specifically oriented [18] particles. Very recently, polynomial fits to HITRAN absorption cross-section data [19] were developed to allow simulations with a large number of halocarbon species [20].

In general, ARTS release versions have an even last digit, development versions an odd last digit. The most recent ARTS overview paper was [21], describing Version 2.2, and this article is about Version 2.6. The most user-visible change between these versions is the Python integration, but there also have been numerous other improvements, such as a new core to calculate atmospheric absorption, updates to the clear-sky radiative transfer core, new scattering solvers, and the capability to do optimal estimation retrievals inside ARTS. Tables 1 and 2 concisely list the most notable changes from 2.2 to 2.4 (Table 1) and from 2.4 to 2.6 (Table 2).

Key changes between 2.2 and 2.4	Other changes worth mentioning
• New improved format for line-by-line data • Non-LTE (pure-rotational non-overlapping, and non-chemical cases) • Dedicated methods for heating rate calculations (see Section 5) • Basic simulations of radars (both single and multiple scattering, see Section 4.2.2) • Radio link calculations not supported in this version • Interfaces to DISORT and RT4 scattering solvers (see Section 4.2) • Jacobian for new quantities: spectroscopic variables and particle properties (hybrid solver, see Section 4.2) • Optimal estimation inversions inside ARTS (see Section 6) • TELSEM and TESSEM surface models • PyARTS: Python bindings for ARTS	• Radiative transfer code (except Monte Carlo) completely revised, including: higher consistency between modules, higher calculation efficiency, Jacobian of atmospheric variables now fully analytical • Absorption code revised: support for new line shapes, performance improvements (see Section 3) • New and extended system for defining particle size distributions (see Section 4.1) • DOIT scattering solver improvements: optimized pressure grid, convergence acceleration, optional precalculated first-guess field • New sensor setup for passband-type meteorological millimeter instruments (sensor_responseMetMM) • New single scattering database for randomly oriented [17] and specifically oriented [18] ice particles

Table 1: Changes between ARTS 2.2 (described in last overview paper [21]) and ARTS 2.4 (last release).

Key changes between 2.4 and 2.6	Other changes worth mentioning
• Extension to shortwave radiation (see Section 2.2), including new clear-sky solver with support for shortwave radiation (iyClearsky), and addition of molecular scattering (clear-sky Rayleigh scattering) • Support of measured cross-section data (e.g. HITRAN absorption cross-sections, see [20] for details) • Improved DISORT interface • Much improved Python integration, including examples (see Section 1.4)	• Improved flux calculations with DISORT (faster, easier and more accurate) • Recent Rosenkranz absorption models added (PWR2021) • MT_CKD 4.0 Water continuum added • Automatic download of ARTS spectral line catalog (see example in Section 1.4) • New workspace method surfaceFlatRvRhEvEh, to calculate 'surface_rmatrix 'and 'surface_emission' when emissivity and reflectance are provided externally.

Table 2: Changes between ARTS 2.4 (last release) and ARTS 2.6 (this version).

1.3. ARTS use — literature analysis

It is interesting to see for what applications ARTS is used in practice. For this, we did a search on Web of Science for all articles that cite one of the three primary ARTS papers [21, 12, 5], between 2018 and June 2023. This yielded 134 publications. Out of these, 29 just mention the program. Often they are about other radiative transfer software (for example [22, 23]) or spectroscopy (for example [24, 25]).

The remaining 105 publications actually used ARTS for their work. The largest group of these (52 publications) deals with remote sensing of the clear atmosphere (without scattering in the radiative transfer setup). Out of these, many used ground-based microwave radiometers for profiles of atmospheric trace gases and temperature. Examples include tropospheric water [26], stratospheric and mesospheric water [27, 28, 29, 30], stratospheric and mesospheric ozone [31, 32, 33, 34, 35], mesospheric carbon monoxide [36, 37, 38], temperature [39, 40], and wind [41, 38].

Another significant group, still within the clear-sky category, are publications with existing or planned satellite sensors, with examples including operational meteorological microwave and infrared sounders [42, 43, 44, 45, 46, 47, 48, 49, 20] and microwave to infrared limb sounders [50, 51, 52, 53, 54, 55, 56, 16]. In addition to these, yet another interesting clear-sky application is the retrieval of the rotational temperature from stratospheric and lower thermospheric O_2 airglow emissions [57, 58].

The other big group of publications that used ARTS (38 publications out of 105) deals with all-sky observations of the atmosphere and/or the retrieval of hydrometeor properties, so they require radiative transfer simulations with scattering. Applications here include passive microwave to sub-mm wave sensors, radars, and their synergy [59, 60, 61, 62, 63, 64, 65, 66, 67, 68, 69, 70, 71, 72, 73, 74]. ARTS is here not only used on its own, but also as a reference to train or validate faster more approximative models, in particular for data assimilation in numerical weather prediction [e.g., 75, 47]. Many studies are in preparation of the upcoming Ice Cloud Imager (ICI) mission on Metop Second Generation [76, 77, 78, 79]. Also, several focus specifically on polarised observations [17, 80, 18, 81]. Other studies focus on terahertz sensors [82, 83, 84, 85, 86] or on infrared sensors [87].

A growing application area is the simulation of atmospheric infrared energy fluxes and associated heating rates in the context of climate modeling [20, 88, 89, 90, 91]. Although ARTS so far was not capable of simulating

radiative transfer in the solar part of the spectrum, a few studies used its capability to compute atmospheric absorption at these frequencies [92, 93, 94].

The overwhelming majority of use is for Earth, but there are also reported applications for Venus [95] and Mars [96]. Also, while the overwhelming majority of studies is in the context of atmospheric science, there is reported use for retrieving surface temperature [97, 98].

In summary, ARTS has been used for a wide range of applications. The vast majority are remote sensing applications, with atmospheric energetics picking up in recent years. Applications with and without scattering are almost equally frequent, with a slight majority for clear-sky. A big majority of applications is passive, but radar also plays a certain role [62, 69, 60].

In terms of frequency region, microwave to sub-mm applications were most common, terahertz and infrared applications were less frequent, and solar applications rare (as expected). This distribution aligns well with the historical development of ARTS, which started as a microwave program and over the years expanded to higher and higher frequencies.

1.4. Python integration

In order to allow the widest possible range of different absorption and radiative transfer simulations, ARTS uses the concept of workspace variables (which hold quantities of interest, such as a vector of simulation frequencies) and workspace methods (which operate on the workspace variables to for example calculate absorption). In the past, calculations were specified in ARTS' own – quite primitive – scripting language. This is still possible, but for most users it will be much more convenient to use pyarts, the new Python interface to these workspace variables and methods, and thus specify the calculation in the form of a Python script.

It is worth pointing out here, that pyarts and ARTS really are the same program. Pyarts just is the name of the Python module. The C++ header library pybind11 [99] is used to automatically generate Python interfaces to the C++ workspace methods. So, pyarts is not ARTS translated to Python, but a python interface to the C++ ARTS methods, and the ARTS workspace.

To work with ARTS in Python, the user has to import module pyarts and create an object of type Workspace. Workspace variables and methods are simply member variables and member functions of that object.

Just enter the name of a workspace variable in an interactive Python session to see its content, or use Python's print() function. In some cases, you may have to append '.value' after the variable name to access its contents.

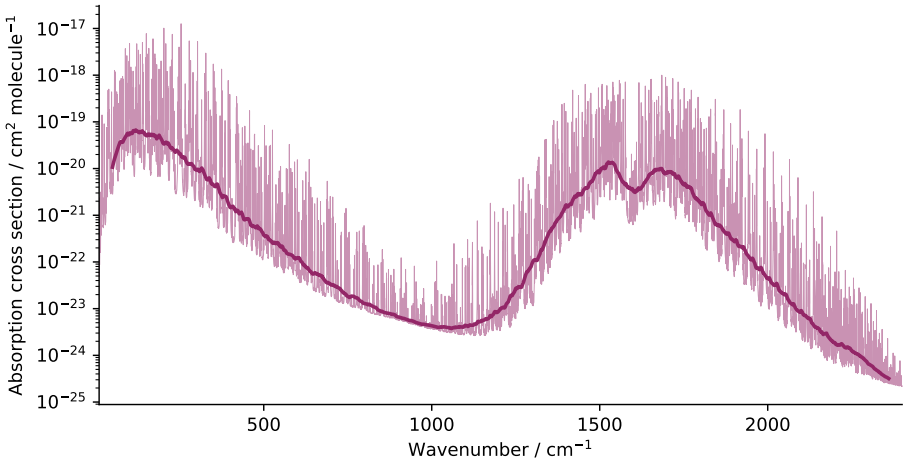

Figure 1: Absorption cross section of water vapor computed with the Python code in Table 3. The heavy line is a geometric running mean (averaging logarithmic values consistently with the plot's logarithmic scale).

In the ipython shell, type a question mark at the end of a workspace method or variable name to see its built-in documentation. You can also find it online on the ARTS homepage.

An overall design goal for pyarts was that it should feel 'pythonic' — natural for any user familiar with other python packages. Pyarts allows all computations that the traditional interface allowed, but with much greater convenience and flexibility. We therefore recommend to use this new interface, even though the old one is still maintained for now (it may be phased out at some point in the future). To ease the transition, we provide also a simple method that parses traditional ARTS controlfiles and translates them into python.

To convey a flavor of how it is to use pyarts, Table 3 gives a complete code example, which computes the absorption cross section spectrum of water vapor and displays it in a simple plot, shown in Figure 1.

In Code Section 1, it is made sure that the ARTS spectral line catalog is available (if not, it is downloaded automatically), and then the ARTS workspace object is created.

Code Section 2 deals with specifying the absorption species to consider, in this case the line-by-line spectrum of water vapor according to the ARTS

```python
import matplotlib.pyplot as plt
import numpy as np
import pyarts

# 1) Prepare ARTS workspace
pyarts.cat.download.retrieve()  # Download ARTS catalogs and set search path
ws = pyarts.workspace.Workspace()  # Initialize ARTS

# 2) Set up absorption species and read catalog data
ws.abs_speciesSet(species=["H2O, H2O-SelfContCKDMT400, H2O-
    ForeignContCKDMT400"])
ws.ReadXML(ws.predefined_model_data, "model/mt_ckd_4.0/H2O.xml")
ws.abs_lines_per_speciesReadSpeciesSplitCatalog(basename="lines/")
ws.abs_lines_per_speciesCutoff(option="ByLine", value=750e9)

# 3) Set up line-by-line calculation
ws.lbl_checkedCalc()  # Check that the line-by-line data is consistent
ws.propmat_clearsky_agendaAuto()  # Set up propagation matrix calculation

# 4) Initialize required workspace variables
ws.stokes_dim = 1  # Unpolarized
ws.jacobian_quantities = []  # No derivatives
ws.select_abs_species = []  # All species
ws.rtp_mag = []  # No magnetic field
ws.rtp_los = []  # No particular LOS
ws.rtp_nlte = pyarts.arts.EnergyLevelMap()  # No NLTE

# 5) Set up the frequency grid and the atmospheric conditions
f_grid_kayser = np.linspace(10, 2400, 30000)  # Frequency grid in Kayser
ws.f_grid = pyarts.arts.convert.kaycm2freq(f_grid_kayser)  # Convert to Hz
ws.rtp_pressure = 1000e2  # 1000 hPa
ws.rtp_temperature = 295  # At room temperature
ws.rtp_vmr = [0.02]  # H2O VMR

# 6) Calculate the absorption cross section
ws.AgendaExecute(a=ws.propmat_clearsky_agenda)  # Call the agenda
xsec = ws.propmat_clearsky.value.data.flatten() / (
    ws.rtp_vmr.value[0] * ws.rtp_pressure.value
    / (pyarts.arts.constants.k * ws.rtp_temperature.value)
) * 10000  # Convert absorption coefficients to cross sections in cm^2

# 7) Plot the absorption of this example
fig, ax = plt.subplots(figsize=(8, 4))
ax.semilogy(f_grid_kayser, xsec, lw=0.2, alpha=0.5, color="#932667")
def rolling_mean(x, w=1000):
    return np.convolve(x, np.ones(w) / w, "valid")
ax.semilogy(rolling_mean(f_grid_kayser), 10 ** rolling_mean(np.log10(xsec)),
     lw=2, color="#932667")
ax.set_xlabel("Wavenumber / cm$^{-1}$")
ax.set_ylabel("Absorption cross section / cm$^2$ molecule$^{-1}$")
ax.set_xlim(f_grid_kayser.min(), f_grid_kayser.max())
ax.spines[["right", "top"]].set_visible(False)
fig.savefig("h2o-xsec.pdf")
plt.show()
```

Table 3: Python example to compute and display the absorption cross section of water vapor.

catalog (based on HITRAN), and the MT_CKD 4.0 self- and foreign continuum of water vapor [100]. It also sets the correct cutoff to the lineshape function for the line spectrum, which is very important in order to get correct total absorption when the continuum models are used. (This procedure is explained in numerous articles, for example in the historical overview by Shine [101].) Note that ARTS uses SI base units throughout, so the canonical cutoff value of $25\,\mathrm{cm}^{-1}$ becomes 750e9 Hz. All function calls in this code section are calls of ARTS workspace methods (which have detailed descriptions in the ARTS online documentation).

Code Section 3 sets up how to actually compute the absorption. The workspace method propmat_clearsky_agendaAuto, which is new in this ARTS release, is very convenient for this. It creates an agenda with just the right workspace methods for the task, based on the selection of absorption species in the workspace variable abs_species, which was set in the previous code section.

Code Section 4 deals with some workspace variables that are needed for advanced features, such as the magnetic field, which is used for calculations with Zeeman splitting. Here we just set them all to empty, because we do not want to use them in this calculation.

Code Section 5 defines the input quantities for our calculation, that is, pressure, temperature, the volume mixing ratio of water vapor, and also the frequency grid. The latter is set first in wavenumber units (Kayser) then converted to the ARTS internal SI base unit of Hz. This is a nice example illustrating the convenience of using python as the control language: The conversion is done by a lower level helper function, not a a workspace method, that is also exposed to Python by pybind11. Note that one could also simply program the conversion, or any other transformations that one might want to apply, in Python directly.

Code Section 6, finally, does the actual calculation. The agenda that was built automatically in Code Section 3 is executed, and it stores its results in the workspace variable for the propagation matrix $\mathbf{K}$, called propmat_clearsky (more on $\mathbf{K}$ in the next section).

In this case, because the workspace variable stokes_dim was set to 1 in Code Section 4, $\mathbf{K}$ contains only a single element (see Equation 4), corresponding to the extinction coefficient (here identical to the absorption coefficient, since there is no scattering).

We then extract that value, convert it from an absorption coefficient to an absorption cross section, and store it in the variable xsec. For the unit

conversion, we divide by the product of volume mixing ratio and total number density (which we compute from pressure and temperature using the ideal gas equation). Normal Python functionality comes handy for this transformation also. A factor 10^4 comes from the conversion from m^2 (SI base unit) to the more conventional cm^2 that we use for plotting.

In Code Section 7, all that is left to do is to create the line plot that is displayed in Figure 1, using Python's powerful matplotlib module.

Hopefully, this quite explicit example helps to convey a feeling for what can be done with this new radiative transfer tool, by freely mixing the specialized ARTS functions with general python code. For more examples see the ARTS online documentation, in particular 'getting started' there. The location is given in Section 'Obtaining ARTS' at the end of this article.

2. Radiative transfer

2.1. Theory

The core equation for ARTS' internal radiative transfer solver is the vector Schwarzschild equation

$$\frac{\mathrm{d}\vec{\mathrm{I}}}{\mathrm{d}s} = -\mathbf{K}\left(\vec{\mathrm{I}} - \vec{\mathrm{J}}\right) \tag{1}$$

where $\vec{\mathrm{I}}$ is the four component Stokes vector, $\vec{\mathrm{J}}$ is the source term, and $\mathbf{K}$ is the propagation matrix, which describes how the radiation is modified along an infinitesimal path distance $\mathrm{d}s$.

The equation formally looks exactly as the original scalar Schwarzschild equation [102], but has a wider scope, not only because $\mathbf{K}$ is a matrix and $\vec{\mathrm{I}}$ and $\vec{\mathrm{J}}$ are vectors, but also because $\mathbf{K}$ and $\vec{\mathrm{J}}$ include the effect of scattering, whereas Schwarzschild thought only about absorption and thermal emission. The advantage of casting the radiative transfer differential equation in this form is that its integral form is known.

One key implementation difference of ARTS version 2.6 compared to version 2.2 is that it now uses a dedicated data type for the propagation matrix $\mathbf{K}$, which greatly speeds up the calculation of polarized radiative transfer by simplifying both matrix inversions and matrix exponential calculations.

We assume in ARTS and in this subsection that $\mathbf{K}$ and $\vec{\mathrm{J}}$ are approximately constant over a small enough distance $r = |s_{i+1} - s_i|$, where i is some discrete positional index. In fact, we discretize ARTS in a level-by-level manner and both $\mathbf{K}$ and $\vec{\mathrm{J}}$ are simply the average of the surrounding levels when a

layer is constructed, explicitly, $\mathbf{K} = \left(\mathbf{K}_i + \mathbf{K}_{i+1}\right)/2$ and $\vec{\mathrm{J}} = \left(\vec{\mathrm{J}}_i + \vec{\mathrm{J}}_{i+1}\right)/2$. Given this, the transmission through the atmosphere between two positions can be written as

$$\vec{\mathrm{I}}_{i+1} = \exp\left(-\mathbf{K}r\right)\vec{\mathrm{I}}_i \tag{2}$$

when the source term is negligibly small, or

$$\vec{\mathrm{I}}_{i+1} = \exp\left(-\mathbf{K}r\right)\left(\vec{\mathrm{I}}_i - \vec{\mathrm{J}}\right) + \vec{\mathrm{J}} \tag{3}$$

when the source term must be taken into account.

The propagation matrix has in other places been called the extinction matrix or the attenuation matrix. We prefer the term propagation matrix, because this matrix also deals with the effect of Faraday rotation, which just moves energy between different polarization states (higher Stokes components), but does not decrease the total intensity (first Stokes component), so that $\mathbf{K}$ is not always associated with extinction. The physical unit of $\mathbf{K}$ is m^{-1}.

There are only 7 independent variables in the 4×4 propagation matrix

$$\mathbf{K} = \begin{bmatrix} A & B & C & D \\ B & A & U & V \\ C & -U & A & W \\ D & -V & -W & A \end{bmatrix}, \tag{4}$$

so only these are kept. The Zeeman effect uses all seven components, Faraday rotation only uses the U-component, and all the other line-by-line, continua, and collision-induced-absorption models of ARTS only use the A-component, corresponding to the scalar extinction coefficient for unpolarized radiation, which would be the sum of absorption coefficient and scattering coefficient.

The matrix exponential $\exp\left(-\mathbf{K}r\right)$ is computed after a rewrite as

$$\exp\left(-Ar\right)\exp\left(\mathbf{K}^{'}\right), \tag{5}$$

where $\mathbf{K}^{'}$ is as Equation 4 but with $A = 0$ and scaled already by r (this is the same solution as found in [103]). We can rewrite the remaining matrix exponential using the Cayley-Hamilton theorem as

$$\exp\left(\mathbf{K}^{'}\right) = c_0\mathbf{I} + c_1\mathbf{K}^{'} + c_2{\mathbf{K}^{'}}^2 + c_3{\mathbf{K}^{'}}^3, \tag{6}$$

where c_0-c_3 are four coefficients that can be found using eigenvalue decomposition. The eigenvalues (λ) are found from solving the characteristic polynomial,

$$\begin{aligned} 0 &= \lambda^4 + b\lambda^2 + c \\ b &= U^2 + V^2 + W^2 - B^2 - C^2 - D^2 \\ c &= -(DU - CV + BW)^2 \\ s &= \sqrt{b^2 - 4c} \\ x^2 &= \sqrt{\tfrac{s-b}{2}} \\ y^2 &= \sqrt{\tfrac{s+b}{2}}, \end{aligned} \tag{7}$$

where x^2 and y^2 are the positive and negative parts of the solutions for λ^2, respectively, as their practical real values. The coefficients of Equation 6 are found from the set of equations

$$\begin{array}{lcccccccc} e^{x} & = & c_0 & + & c_1 x & + & c_2 x^2 & + & c_3 x^3 \\ e^{-x} & = & c_0 & - & c_1 x & + & c_2 x^2 & - & c_3 x^3 \\ e^{iy} & = & c_0 & + & ic_1 y & - & c_2 y^2 & - & ic_3 y^3 \\ e^{-iy} & = & c_0 & - & ic_1 y & - & c_2 y^2 & + & ic_3 y^3 \end{array} , \tag{8}$$

which yields

$$c_0 = \frac{x^2 \cos y + y^2 \cosh x}{x^2 + y^2} \tag{9}$$

$$c_1 = \frac{x^2 \frac{\sin y}{y} + y^2 \frac{\sinh x}{x}}{x^2 + y^2} \tag{10}$$

$$c_2 = \frac{\cosh x - \cos y}{x^2 + y^2} \tag{11}$$

$$c_3 = \frac{\frac{\sinh x}{x} - \frac{\sin y}{y}}{x^2 + y^2}. \tag{12}$$

Lastly, it is important to keep some limits in mind as $x \to 0$ or $y \to 0$ as the hyperbolic and the trigonometric functions are not computationally stable while they are divided by some numbers close to 0. For convenience, these

limits are

$$\begin{aligned}
c_0: &\quad \lim_{x\to 0} c_0 &&= \lim_{y\to 0} c_0 = 1 \\
c_1: &\quad \lim_{x\to 0} c_1 &&= \lim_{y\to 0} c_1 = 1 \\
c_2: &\quad \lim_{x\wedge y\to 0} c_2 &&= \tfrac{1}{2} \\
c_3: &\quad \lim_{x\wedge y\to 0} c_3 &&= \tfrac{1}{6} \\
&\quad \lim_{x\to 0} c_3 &&= \tfrac{1}{y^2} - \tfrac{\sin y}{y^3} \\
&\quad \lim_{y\to 0} c_3 &&= \tfrac{\sinh x}{x^3} - \tfrac{1}{x^2},
\end{aligned} \tag{13}$$

where $x \wedge y \to 0$ means that both variables approach zero. We have opted for a value of 0.001 as a limit of actual 0 of x and y.

As a comment on the numerics of this matrix exponential solution, we are not sure how stable the method really is, but it is very fast. The work by Moler and Van Loan [104] gives the scaling and squaring method with the Padé approximation as one of the most effective algorithms at hand. The algorithm above is more than an order of magnitude faster in our experience.

The differences between the methods in computed results are small if the maximum value in $\mathbf{K}'$ is small (less than 0.1) but grow out of control if this is large (above 10). We cannot judge which method is then better, but we do note that the Padé approximation algorithm tends to return infinities when the algorithm above still returns large but finite values. In any case, since an atmospheric layer with too much absorption is a poorly designed atmospheric layer, for the sake of radiative transfer using the faster algorithm above is simply better.

The source function is first computed as

$$\vec{\mathrm{J}} = \mathbf{K}^{-1}\left(\vec{\alpha}B_P + \vec{\mathrm{J}}_n + \vec{\mathrm{J}}_s + \vec{\mathrm{J}}_\odot\right), \tag{14}$$

where $\vec{\alpha} = \{A, B, C, D\}^\intercal$ is the absorption vector, B_P is Planck's function, $\vec{\mathrm{J}}_n$ is the emission correction due to non-local thermodynamic equilibrium, $\vec{\mathrm{J}}_s$ is the additional particulate scattering source term, and $\vec{\mathrm{J}}_\odot$ is the additional solar scattering term.

When the atmosphere is in local thermodynamic equilibrium, and there is no Sun, and scattering is not considered, this simply translates to $\vec{\mathrm{J}} = \{B_P, 0, 0, 0\}^\intercal$. This can be seen from noting that $\mathbf{K}^{-1}\mathbf{K}$ is the unit matrix and $\vec{\alpha}$ is just the first column of $\mathbf{K}$. The $\vec{\mathrm{J}}_n$ is computed as the additional emission caused by non-local thermodynamic equilibrium added up for every

absorption species. Note also that the split above is done mostly for pedagogical reasons. Inside ARTS $\vec{\mathrm{J}}_n$ and $\vec{\mathrm{J}}_s$ are treated as the same variable, but $\vec{\mathrm{J}}_\odot$ is still treated separately.

The background source term, $\vec{\mathrm{I}}_0$, depends on the background of the propagation path. Three such backgrounds are allowed: (1) surface, (2) space, and (3) a cloud box. The surface in particular might itself recursively spawn a new set of radiative transfer calculations to compute the incoming radiation. For propagation paths with space as background, the sun is added as background source if the propagation path in reverse direction hits the solar disc. This allows to resolve the shape of the sun or to track the sun through the atmosphere.

2.2. Simulations with a solar source term

In this subsection we will give a brief overview about simulations with a solar source. There will be also an upcoming article dedicated to this. The simulation of solar radiation in ARTS is based on the assumption that the distance between the Sun and any position within the atmosphere or on the surface is much larger than the radius of the Sun. This means that the angular variability of radiation leaving the surface of the Sun can be neglected and the incoming spectral radiance is assumed to be parallel (collimated beam approximation, [105]). For a position at the top of the atmosphere (TOA), the incoming spectral radiance (in units of $\mathrm{W\,m^{-2}\,sr^{-1}\,Hz^{-1}}$) in direction Ω at TOA can be described as

$$I_{s,TOA}\left(\Omega\right) = F_{s,TOA}\delta\left(\Omega - \Omega'\right) \tag{15}$$

with Ω' the direction from the center of the Sun to TOA and $F_{s,TOA}$ the spectral irradiance (in units of $\mathrm{W\,m^{-2}\,Hz^{-1}}$) at TOA and δ the Dirac function. The spectral irradiance $F_{s,TOA}$ at TOA is

$$\begin{aligned} F_{s,TOA} &= \int_0^{2\pi}\int_0^{\alpha_{s,TOA}} I_s \cos\theta \sin\theta \mathrm{d}\theta\mathrm{d}\phi \\ &= \pi I_s \sin^2\alpha_{s,TOA} \\ &= F_s \sin^2\alpha_{s,TOA}\,, \end{aligned} \tag{16}$$

with $\alpha_{s,TOA}$ the solar angular radius at TOA, F_s the solar spectral irradiance at the position of the Sun in space and I_s the hemispherically isotropic radiance leaving the surface of the Sun. The factor $\sin^2\alpha_{s,TOA}$ takes into account

that the irradiance is changing with the inverse square of the distance as it is

$$\sin^2 \alpha_{s,TOA} = \frac{r_s^2}{d_{s,TOA}^2 + r_s^2} \tag{17}$$

with r_s the radius of the sun and $d_{s,TOA}$ the distance between TOA and the center of the sun. Inserting (16) in (15) results in

$$I_{s,TOA}(\Omega) = F_s \sin^2 \alpha_{s,TOA} \delta(\Omega - \Omega') \tag{18}$$

This approach makes it possible to use the same solar spectrum for different distances of the sun, for example to simulate radiation for different planets or different orbital configurations. The only thing, that needs to be changed is the actual distance between the sun and the planet. The incoming spectral radiance is automatically adjusted. Note that F_s is formally defined at the center of the sun, although it could of course never be observed there. At the surface of the sun I_s is already reduced by a factor of 1/2, according to Equation 17.

ARTS assumes an elliptical geometry. This has some implications compared to a plane parallel geometry. For example, the distance between the sun and TOA is not unique but depend on the geographical position. In Figure 2 the distance R_A at TOA location A is greater than the distance R_B at TOA location B. This also results in different angular radii, because the angular radius α_s depends on the distance. The resulting differences due to the different geographical positions are small, in the order of 0.1 W m^{-2}, but they can be important for reference simulations, especially when comparing to simulations with other geometries. Furthermore, the direction Ω' from the sun to TOA depends on the geographical position because the radiative transfer is relative to a local coordinate system. For example, the local solar incidence angles Θ_A and Θ_B in Figure 2 differ, which results in different directions Ω'.

In addition to the irradiance spectrum, a solar source is defined by the radius of the Sun, its distance to the planet and the geographical position where the Sun is at zenith on the planet. A solar spectrum can be defined as a black body with an effective emission temperature or as an arbitrary user-defined spectrum.

There are two solvers in ARTS capable of simulations with a solar source term: First, there is ARTS' internal clear-sky solver iyClearsky. It is a 3D fully polarized radiative transfer solver for spherical geometry. It includes

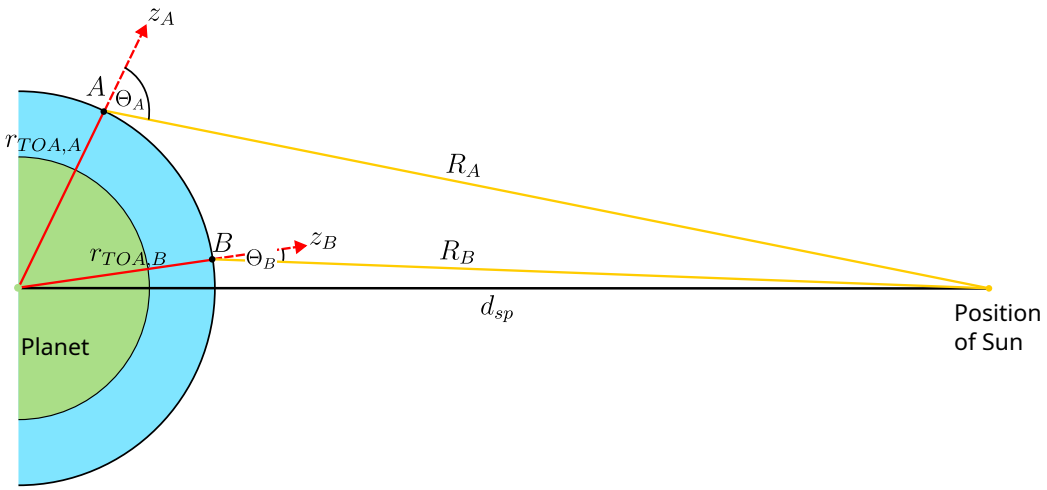

Figure 2: Sketch of the sun planet geometry. R_A and R_B are the distance from the TOA locations A and B to the sun. $r_{TOA,A}$ and $r_{TOA,B}$ are the distance between the center of the planet and the TOA locations A and B. z_A and z_B define the local vertical directions and d_{sp} is the distance between the position of the Sun and the center of the planet.

first order molecular scattering from solar sources but no scattering of particulates or scattering from thermal sources.

Second, there is CDISORT [106], which is DISORT 2.1 [105] ported to C and for simplicity called DISORT from here on. It is a 1D non-polarized radiative transfer solver for plane parallel atmospheres and can handle multiple scattering. In contrast to iyClearsky, DISORT can have only one solar source. As DISORT is a plane parallel solver and ARTS assumes a spherical geometry, it needs to be run for a specific geographic position because the local solar zenith angle, which DISORT internally needs, is calculated from the specific geographic position and the geographic zenith position of the Sun.

For both solvers molecular scattering (Rayleigh scattering) is provided by a parametrization from M. Callan, University of Colorado [105] based on the results of Bates [107] for the scattering cross sections and the Rayleigh phase matrix including depolarization from Hansen et al. [108].

Line shape	Parameters
Doppler	G_D
Lorentz	G_0, D_0
Voigt	G_D, G_0, D_0
Speed-dependent Voigt	G_D, G_0, D_0, G_2, D_2
Hartmann-Tran	G_D, G_0, D_0, G_2, D_2, f_c, η

Table 4: Summary of available line shape operators in ARTS and their input parameters. G_D is the Doppler width, G_0 is the speed-independent pressure width, D_0 is the speed-independent pressure frequency shift, G_2 is the speed-dependent pressure width, D_2 is the speed-dependent pressure frequency shift, f_c is the frequency of velocity changing collisions, and η a correlation factor. Except for G_D, the other parameters depend on temperature as detailed in Table 5. See Tran et al. [109] for details, we follow them in our definitions.

3. Absorption

3.1. Computing absorption from spectroscopic data

How ARTS computes absorption coefficients by summing up spectral lines based on spectroscopic data has been completely re-implemented. The set of operators and multiplications for each spectral line is

$$\alpha = (1 + G_{lm} - iY_{lm})\, S(T, p, \cdots) N(\nu, \cdots) F(\nu, \cdots), \tag{19}$$

where α is the complex absorption coefficient, whose real part is the attenuation and imaginary part is the dispersion. The G_{lm} and Y_{lm} parameters are the second and first order line mixing coefficients, the S operator computes the line strength, the N operator renormalizes the line shape, and the F operator computes the line shape. Furthermore, i is the imaginary unit, T is temperature, p is pressure, and ν is frequency.

There are many variants and combinations of these operators available. For the line shape F, Table 4 gives a summary of available operators and what user input they depend on, and Table 5 lists what temperature dependence models for these parameters are supported.

As one example, the adaptation of default HITRAN line-by-line data for ARTS [24] uses

$$\alpha = \frac{x_s p}{kT} S_i \frac{Q(T_0)}{Q(T)} \exp\left(E_i \frac{T - T_0}{kTT_0}\right) \frac{\nu \left(\exp\left[h\nu/kT\right] - 1\right)}{\nu_i \left(\exp\left[h\nu_i/kT_0\right] - 1\right)} F_v(\cdots), \tag{20}$$

Model	Formulation
T0	X_0
T1	$X_0 \left(\frac{T_0}{T}\right)^{X_1}$
T2	$X_0 \left(\frac{T_0}{T}\right)^{X_1} \left[1 + X_2 \log\left(\frac{T}{T_0}\right)\right]$
T3	$X_0 + X_1(T - T_0)$
T4	$\left[X_0 + X_1 \left(\frac{T_0}{T} - 1\right)\right] \left(\frac{T_0}{T}\right)^{X_2}$
T5	$X_0 \left(\frac{T_0}{T}\right)^{0.25+1.5X_1}$
AER	$X(T = 200) = X_0$, $X(T = 250) = X_1$, $X(T = 296) = X_2$, $X(T = 340) = X_3$, linear interpolation
DPL	$X_0 \left(\frac{T_0}{T}\right)^{X_1} + X_2 \left(\frac{T_0}{T}\right)^{X_3}$
POLY	$X_0 + X_1 T + X_2 T^2 + X_3 T^3$

Table 5: Temperature dependence of line shape parameters in Table 4. The names are as enumerated inside ARTS. The coefficients that are provided by the user are X_0, X_1, X_2, and X_3. T is the current temperature and T_0 is the reference temperature.

where the terms before the $F_v(\cdots)$ line profile operator represent the S and N operations of Equation 19, x_s is the volume mixing ratio of the molecule in question, k is Boltzmann's constant, S_i is the reference line strength of the absorption line as provided by HITRAN, Q is the total internal partition sum operator for some temperature [110], T_0 is the reference temperature of the line (for HITRAN always 296 K), E_i is the HITRAN lower state energy level of the absorption line, ν is the frequency at which absorption is sampled, ν_i is the HITRAN reference line center of the absorption line, and h is the Planck constant. HITRAN does not provide any line mixing parameters by default, so the $1 + G_{lm} - iY_{lm}$ term of Equation 19 disappears completely.

The $F_v(\cdots)$ line profile operator in this example case is

$$F_v(\cdots) = \frac{1}{\sqrt{\pi} G_D} w\left(\frac{\nu - \nu_i - D_0 + G_0}{G_D}\right) \tag{21}$$

$$G_D = \frac{\nu_i}{c}\sqrt{\frac{2000RT}{m_s}} \tag{22}$$

$$G_0 = x_s \gamma_{i,s} p \left(\frac{T_0}{T}\right)^{n_{i,a}} + (1 - x_s)\,\gamma_{i,a} p \left(\frac{T_0}{T}\right)^{n_{i,a}} \tag{23}$$

$$D_0 = \delta\nu_{i,a} p \tag{24}$$

where w is the Faddeeva function (the convolution of the Doppler line profile and the Lorentz line profile [111]), c is the speed of light, m_s is the molar mass of the molecule in question, R is the universal gas constant, $\gamma_{i,s}$ is the HITRAN self broadening coefficient, $\gamma_{i,a}$ is the HITRAN air broadening coefficient, $n_{i,a}$ is the HITRAN air broadening temperature exponent, and $\delta\nu_{i,a}$ is the HITRAN air pressure shift. In Equation 22, a factor 1000 comes in because we give the molar mass m_s in grams per mole, and R and T in SI units (as all other quantities).

Comparing the expressions of Equations 21 to 24 to Tables 4 and 5 shows that with the standard HITRAN data we are using a Voigt line shape with the T1 temperature model for the parameters going into the pressure width G_0 and the T0 temperature model for the parameter going into the pressure shift D_0.

By default, HITRAN does not provide the more complete Hartmann-Tran profile parameters [109], but ARTS can in principle compute the Hartmann-Tran profile if the parameters are supplied. For this the users must provide

the parameters listed in the last row of Table 4 in a form fitting on of the temperature models of Table 5 and set the appropriate line profile operator.

One additional complication not covered by any of the expressions above occurs when the atmosphere is considered in non-local thermodynamic equilibrium as this will contribute to the $\vec{J}_n$ term of Equation 14. Yamada et al. [112] describes the basics of the implementation in ARTS to compute non-local thermodynamic equilibrium.

3.2. Other absorption

Besides spectral line by spectral line absorption calculations, ARTS also includes state of the art absorption continua, such as CKD_MT up to Version 4 for water vapor (from Version 4 on CKD_MT water vapor continuum coefficients are stored as external data and distributed via the HITRAN website, so any later version will also work). Furthermore, HITRAN collision-induced absorption ([113], last HITRAN data access July 2022) and absorption cross section data [19] are also available, for example for halocarbons as described in [20]. Continua and other absorption functions will continue to be updated as new data become available.

4. Scattering

This section deals with simulations where scattering by particles within the atmosphere is considered. Particles here refers to hydrometeors (liquid or frozen cloud and precipitation particles) or aerosols. ARTS 2.6 handles for the first time also molecular scattering (for UV/visible radiation) but this is to be described in another article. This section starts by outlining the input data required, and ends with an overview of available scattering solvers.

4.1. Particle properties

The combination of shapes and sizes of aerosols and hydrometeors is basically unlimited and, as a consequence, the core manner in ARTS to describe particle properties is generic by design. It is up to the user to decide what set of scattering elements to include in the calculations. The definition of a scattering element has two parts, the single scattering properties of the element and the associated number density.

4.1.1. Single scattering data

ARTS has its own format for single scattering data. These data represent the extinction, absorption and scattering function, gridded as a function of frequency and temperature, of the scattering element. For a limited set of shapes, including spheroids and cylinders, the single scattering data can be calculated with a relatively low calculation burden by the T-matrix method. ARTS contains an interface to such code, the one by [114]. For more complex shapes, the scattering data have to be calculated externally. For hydrometeors and calculations at frequencies between 1 and 900 GHz, the ARTS infrastructure contains an extensive database of precomputed values. This ARTS single scattering database consists of two parts. The broadest selection of habits (i.e., shape model) is offered for the standard assumption of totally random orientation (TRO), for details see [17]. The ARTS format can also represent particles that just have azimuthally random orientation (ARO). The corresponding part of the database contains data for two habits [18]. Data from other databases covering cloud ice particles have been converted to the ARTS format and been applied. We are not aware of any application of ARTS involving scattering by aerosols, but this should in principle also be possible.

4.1.2. Particle number densities and size distributions

The user can opt to directly import particle number densities for the chosen scattering elements, if such are at hand from an external source or are calculated on the Python side. However, more common is the case that the user has bulk properties, such as condensate mass concentrations, and from this wants to generate particle number concentrations that follow a particle size distribution (PSD). To simplify this process, a number of PSD parameterisations are included in ARTS. For clarity, it should be noted that a PSD is a continuous size distribution (for example in units of $\#/(\mathrm{m}^3 \cdot \mathrm{m})$), while derived particle number densities are values integrated/binned in size (for example in units of $\#/\mathrm{m}^3$).

First of all, there is a set of methods for treating the PSD as a modified gamma distribution (MGD), implemented following the nomenclature and equations of [115]:

$$n(x) = N_0 x^{\mu} e^{-\Lambda x^{\gamma}}, \tag{25}$$

where the four MGD parameters are N_0, μ, Λ, and γ, and x is the measure on size. To allow analytical expressions for all needed operations, the

relationship between size and mass must follow a power-law:

$$m = ax^b. \tag{26}$$

As long as Equation 26 can be fulfilled, x can represent any selection of size. For example, to let x represent mass, both a and b have to be set to 1. See [115] for further choices.

The MGD methods allow that N_0, μ, Λ and γ all vary throughout the atmosphere, but can also be set to be constant. That is, the user can operate with up to four moments. There are methods for expressing one moment as bulk mass [kg/m^3], possibly combined with a second bulk property. This second moment can be number density, mean particle mass, mean size or median size. There is also a MGD method handling the common assumption of a power-law relationship between N_0 and Λ. The generic PSD methods include also two methods for setting up mono-dispersive distributions.

There are several PSD methods specific for hydrometeors. For rain the PSDs of [116] and [117] are included. The classical rain PSD of [118] is covered by the general MGD methods. For ice hydrometeors, the parameterisations of [119], [120], [121] and [122] are included. Also included are two PSD schemes matching multimoment microphysics schemes common in atmospheric models [123, 124].

All these methods can provide the derivative of the PSD with respect to free parameters (that is, the moments used). This is a prerequisite to perform OEM inversions of observations involving scattering. However, just two of the scattering solvers can actually use this feature, see below.

4.2. Scattering solvers

Algorithms performing radiative transfer in the presence of scattering are referred to as scattering solvers. Common to these algorithms is that they solve the problem that, due to scattering, radiation traveling in a given direction depends on the radiation in all other directions at the same point. Expressed in the mathematics of section 2.1, the computation of the $\vec{\mathrm{J}}_s$ term in Equation 14 would require an integral over the radiation Stokes vector $\vec{\mathrm{I}}$ from all incoming directions, weighted by the scattering phase matrix, making the simple solution of integrating along a single line of sight, as in Equation 3, impossible.

Different scattering solvers employ different strategies to overcome this. In doing so, they use their own internal representation of the radiation field,

Name	Vector	3D	PP	Flux	Comment
DISORT	No	No	Yes	Yes	Only Lambertian surface
DOIT	Yes	Yes	No	Yes	3D not recommended
Hybrid	No	Yes	No	No	Can be used with OEM
MC	Yes	Yes	No	No	Choice for detailed 3D
RT4	Yes	No	Yes	Yes	No multi-threading

Table 6: ARTS radiance scattering solvers. The columns are, starting from left: short name of the solver, if vector (polarized) radiative transfer can be made, if 3D geometry covered, if plane parallel, if suitable for flux calculations, and notable limitation or feature. Solvers having Yes below Vector can also handle particle orientation (ARO). Comments refer to the implementation in ARTS, and should not be taken as generally true in the case of third party solvers.

and their own intrinsic approximations and simplifications, such as scalar (unpolarized) radiation only, one-dimensional atmospheres, and often plane-parallel geometry. It goes beyond the scope of this text to discuss the different solver strategies, good overviews are given for example in [125, 126, 127, 128]. Instead, the goal here is to describe the solvers that are available in ARTS, along with their strengths and limitations, where limitations include those that are intrinsic to the solver and those related to our implementation or the coupling to ARTS.

ARTS comes with two types of scattering solvers, a set for calculating scattering of thermal emission, resulting in radiances, and two methods for simulating radar reflectivity measurements. These are described in separate subsections below.

4.2.1. Radiances

The discrete ordinate iterative (DOIT) [2] and the Monte Carlo (MC) [6] solvers were developed directly for ARTS and were introduced by [12]. More recently, interfaces to two external scattering solvers have been added, namely DISORT and RT4. The MC module is restricted to simulate remote sensing observations, while DISORT, DOIT and RT4 provide the full radiance field and can thus also form the basis for flux calculations (Sec. 5). Table 6 gives a summary of the scattering solvers covered by this section and their individual limitations.

The DISORT approach [129] is arguably the most established scattering solver in our field and exists in several implementations. ARTS is coupled to the code of [106]. In contrast to other scattering solvers in ARTS, DISORT is

limited to unpolarized (scalar) calculations and thus also to totally random particle orientation (TRO).

The RT4 solver [130] fits better with the general functionality of ARTS. It handles polarized radiation and scattering data for both TRO and ARO and it can be coupled to ARTS own description of specularly reflecting surfaces. A limitation of RT4 compared to DISORT is that scaling with respect to the forward scattering peak is missing. RT4 also can not yet be used with multi-threading inside ARTS, mainly as RT4 comes as FORTRAN code.

Both DISORT and RT4 assume a plane-parallel atmosphere (in other words an infinite planet radius), while remaining parts of ARTS operate with a spheroidal reference geoid. Another deviation to ARTS is that RT4 and DISORT take layer-means as input, while ARTS operates with point values (assuming a linear variation, in each spatial dimension, between grid points). To overcome this difference, an averaging is performed between the altitude levels of ARTS. That is, if the ARTS pressure grid has n points, DISORT and RT4 will be used with n-1 layers. This difference in discretization can be significant if comparing radiances between scattering solvers inside ARTS.

To extend the usage of the scattering solvers of 1D character, an independent beam approximation (IBA) wrapper method has been implemented. This method allows to apply the 1D solvers in simulations of remote sensing data done using 2D and 3D atmospheres. The IBA strategy is to calculate the propagation path through the 2D or 3D atmosphere, and interpolate the atmospheric and surface fields to the points of the path. After the interpolation, the obtained values are used to create a, likely slanted, 1D view of the atmosphere. The final radiances for the simulation are obtained by interpolating, in angles, the radiation field given by the scattering solver based on the obtained 1D view. By applying IBA repeatedly it is possible to incorporate inhomogenities inside the footprint of microwave sensors with relatively small errors compared to full 3D MC calculations [72]. For observations resulting in that the propagation path does not cover all altitudes (such as airborne upward observations), the atmosphere is sampled vertically to cover the missing altitude range, starting from the observation point.

None of the scattering solvers mentioned above provides the Jacobian, which is a prerequisite for OEM-type retrievals (see Section 6). As a first step to overcome this limitation, a hybrid method has been implemented. In short, either DISORT, DOIT or RT4 is first run to obtain the full radiance field. The hybrid method performs an integration following Equation 3, where the precalculated radiance field is used to calculate the scattering source term ($\vec{J}_s$

in Equation 14). The general approach for deriving the Jacobian in ARTS has been extended to cover this case, but with the limitation that the incoming radiation field is assumed constant. That is, the provided Jacobian ignores the fact that a change at one point in the atmosphere can affect the scattering source term at another point. Thus the Jacobian is not fully exact, but tests showed that retrieval convergence can be achieved in most cases and the method has been applied successfully in remote sensing applications [68, 69].

The hybrid method is fully integrated into ARTS. The internal functions of ARTS for performing pencil beam radiative transfer have been extended to handle a precalculated scattering source term, as required by the hybrid method. When decreasing the amount of scattering along the pencil beam, the hybrid method converges to the standard clear-sky emission solver. As an internal solver, it operates with a spherical planet. The hybrid approach calculates the radiance and the Jacobian for a specific observation direction. In this sense it is similar to the MC module, in contrast to the other, full, scattering solvers that calculate the full radiation field. Since the hybrid method needs a full radiation field as input, one should see it simply as a way to complement a solution from any of the other ARTS scattering solvers with a Jacobian.

We will end this subsection with a usage example: Fox et al. [131] used ARTS to evaluate the representation of ice clouds in a Numerical Weather Prediction (NWP) model. The Monte Carlo scattering solver was used to simulate passive sub-millimeter wave brightness temperatures from 3D NWP model input fields using ice crystal scattering properties from the ARTS database [17], and these were compared to airborne observations. The flexibility permitted by the wide range of ice crystal habits provided in the ARTS scattering database, and the different PSD parameterisations described above, make it possible to achieve good consistency between the representation of cloud microphysics in the NWP model and radiative transfer simulations.

Figure 3 shows an example of the simulated and observed brightness temperatures between 157 and 874 GHz, and the NWP model hydrometeor fields used as input to the simulations. This example used the scattering properties of the large column aggregate particle type to represent the cloud ice. The study demonstrated that ARTS is capable of simulating realistic brightness temperatures across the full range of frequencies used, when appropriate ice crystal scattering models are selected, although in this example there are some discrepancies, particularly at 664 and 874 GHz in the vicinity

of the convective core. These are probably caused by errors in the NWP hydrometeor fields, although it is also possible that different microphysical assumptions are required in different regions of the cloud.

4.2.2. Radar measurements

ARTS contains two methods for simulating atmospheric monostatic radar observations. Their complexity depends strongly on whether multiple scattering is significant or not. As a consequence, there are two distinct radar methods.

For **single scattering** only simulations, the calculation is very straightforward, and the core task is to determine the bulk backscattering and weigh it with the two-way transmission:

$$\vec{\mathrm{I}}_b = \mathbf{T}\mathbf{Z}_b\mathbf{T}\vec{\mathrm{I}}_t, \tag{27}$$

where $\vec{\mathrm{I}}_b$ is the Stokes vector for the returned radar pulse, $\vec{\mathrm{I}}_t$ is the unit Stokes vector describing the polarisation state of the transmitted pulse, $\mathbf{Z}_b$ is the bulk scattering matrix for the point of concern in the back-scattering direction, and $\mathbf{T}$ is the Mueller transmission matrix for the distance between the radar transmitter/receiver and the backscattering point.

The transmission matrix for the away and return directions can theoretically differ (for vector calculations, not for scalar ones), but this should be of no practical concern and is ignored here. Furthermore, the method allows to scale the extinction going into $\mathbf{T}$. This is a scalar value, r_e, with one as default. By setting $r_e = 0$, the unattenuated return pulse is obtained. At least for some situations, a full calculation with multiple scattering ends up roughly halfways between $r_e = 0$ and $r_e = 1$ [132], and setting $r_e \approx 0.5$ could be considered for approximating the neglection of multiple scattering.

This single-scattering method provides the full Jacobian. That is, the Jacobian includes derivatives with respect to both $\mathbf{Z}_b$ and $\mathbf{T}$. OEM retrievals using this method are found in papers by Pfreundschuh et al. [68, 69].

For **multiple scattering** simulations, the calculation becomes more complex. For simulating atmospheric profiling pulse radar, the calculation of scattering events has to be considered within the context of pulse propagation time. Additionally, to avoid overestimating multiple scattering effects and properly account for the relationship between beam size and multiple scattering, simulations require a finite antenna pattern [133, 134].

Following studies by Marzano et al. and Battaglia et al. [135, 134], ARTS uses a Monte Carlo approach to account for multiple scattering effects from

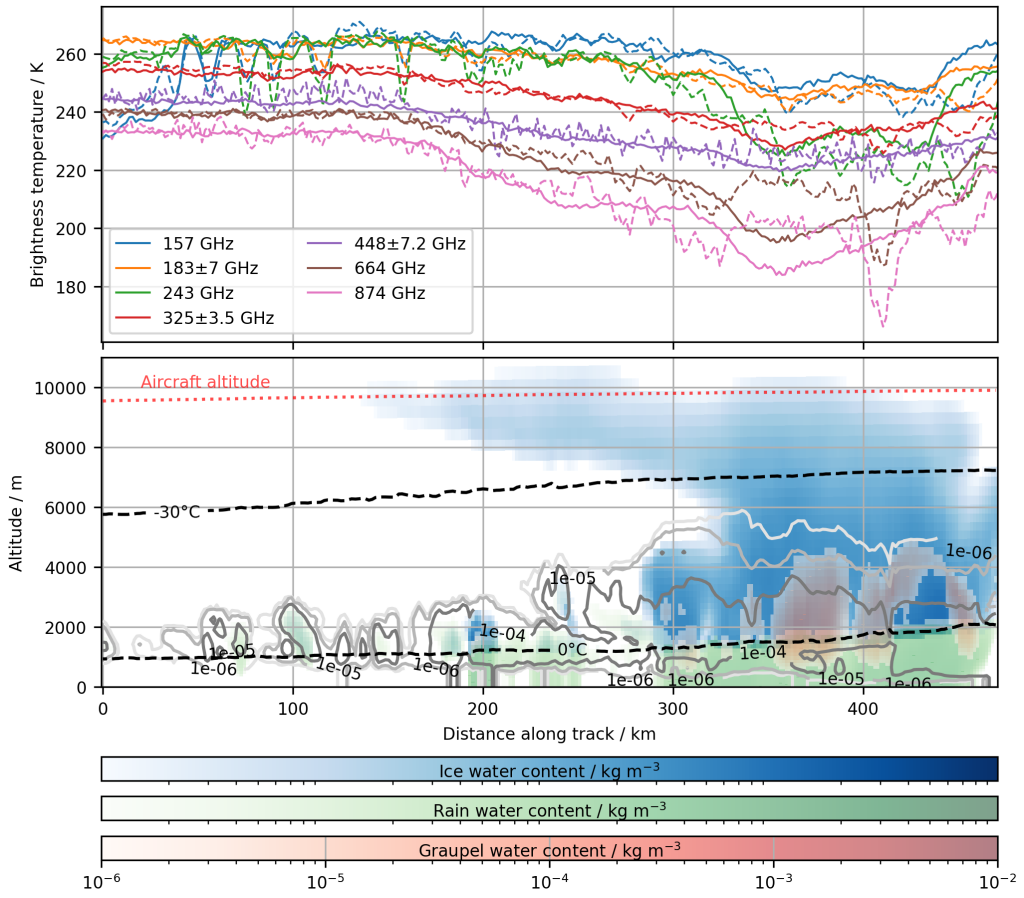

Figure 3: Top panel: Simulated (solid lines) and observed (dashed lines) brightness temperatures between 157 and 874 GHz from a passive airborne radiometer viewing a cloudy scene. Bottom: Cross-section of the cloud fields from the NWP model used as input to the simulations. The colours represent the ice, rain and graupel water contents, and the gray contours represent the cloud liquid water content.

hydrometeors in the atmosphere. All scattering events have the potential to contribute to the simulated backscatter profile, so backward ray tracing would not produce any computational advantage unlike those realized for passive sensing [for example 6]. Therefore, ray tracing initiates from the transmitter using traditional forward Monte Carlo sampling.

Each discrete contribution to the radiative transfer solution is initiated by drawing two random numbers from a bivariate Normal distribution with means aligned with the sensor boresight and standard deviations related to the antenna full-width, half-maximums (FWHM) of the E- and H-planes of the antenna pattern, where $\sigma = FWHM/2.3548$. This procedure determines the direction of the line-of-sight for the radiative transfer contribution under the assumption of a Gaussian antenna pattern.

Next to calculate propagation path length, a random number r_p drawn from a uniform distribution represents the scalar path transmission corresponding to the extinction of the first Stokes element I. Starting with a scalar transmission coefficient $t_I = 1$, the path transmission matrix is accumulated while $t_I > r_p$. For cases in which the bulk extinction matrix is block-diagonal due to contributions from azimuthally-random particles, transmission includes the effects on cross-polarization based on the state of the Stokes vector at the beginning of the propagation path. When $t_I \leq r_p$, propagation ends and the accumulated transmission matrix, and corresponding path length, are stored.

After path length and transmission calculation, the bulk scattering properties are calculated at the propagation path end. A random number r_a is drawn from a uniform distribution and compared with the single scattering albedo α_{ss} (the ratio of scattering cross-section C_{sca} over extinction cross-section C_{ext}). If $\alpha_{\text{ss}} < r_a$, propagation is terminated at an extinction event; otherwise, the monostatic backscatter contribution is recorded for the radar range bin corresponding to the calculated path length. This contribution includes the normalized transmission in the transmit direction, to account for polarization mixing, return transmission, and weighting for the receiver Gaussian antenna pattern.

After accounting for the scattering event, the process restarts, this time with uniform random variables r_{ze} and r_{az} providing the zenith and azimuth scattering directions, and a new starting (scattered) Stokes vector $\vec{\mathrm{I}}_s$ is calculated from the product of the phase matrix $\mathbf{Z}$ and the incident Stokes vector $\vec{\mathrm{I}}_i$:

$$\vec{\mathrm{I}}_s = \mathbf{Z}(\theta_i, \theta_s, \Delta\phi)\vec{\mathrm{I}}_i \tag{28}$$

where θ is the zenith angle and $\Delta\phi$ is the difference of the scattered and incident azimuth angles. Subscripts i and s correspond to incident and scattered, respectively.

At subsequent scattering events, bistatic scattering for the incident and scattered angles contributes to the accumulated backscattering at the range bin corresponding to the total distance traveled before the scattering event. Path tracing ends, at an absorption event, when I falls below a predetermined threshold, or when the maximum specified scattering order is reached. A scattering order of 1 is equivalent to single scattering. For multiple scattering simulations, the suggested scattering order is 20 based on use across a range of cloud types.

Figure 4 shows an example simulation, a hypothetical space-based nadir-pointing W-band radar, comparing single scattering (top panel) and multiple scattering (middle panel) simulations, with differences shown at the bottom. The top simulation uses the ARTS single scattering solver convolved with a Gaussian antenna pattern such that the field of view at the surface is 1 km. As expected, the largest multiple scattering enhancement corresponds to the convective cells and the surrounding regions. Multiple scattering results in excess reflectivity where the W-band signal is otherwise being extinguished, but this large enhancement is decorrelated from the vertical structure of the cloud along the radar line of sight. There are two features to note. The multiple scattering simulations are noisy at cloud edges and miss some thin clouds captured in the single scattering simulation. This is due to the large number of ray traces, on the order of 5e5, needed to resolve the simulations. While runtime is linear with the number of ray traces, the ray tracing routine is not trivial in terms of runtime. Thus, this simulator should be used only when multiple scattering is suspected.

5. Radiative energy flux and heating rate calculations

5.1. Fluxes

ARTS is suitable for accurate reference calculations of atmospheric energetics: radiative energy fluxes and associated heating rates. As an example, Roemer et al. [136] used it to investigate the longwave radiative feedback from a spectrally resolved perspective. To this end, spectral irradiance ($\mathcal{L}_\nu$) at the top of the atmosphere was calculated for a set of idealised atmospheres, using the existing interface between ARTS and the single-column radiative-convective equilibrium model konrad [90, 137]. Figure 5 shows some

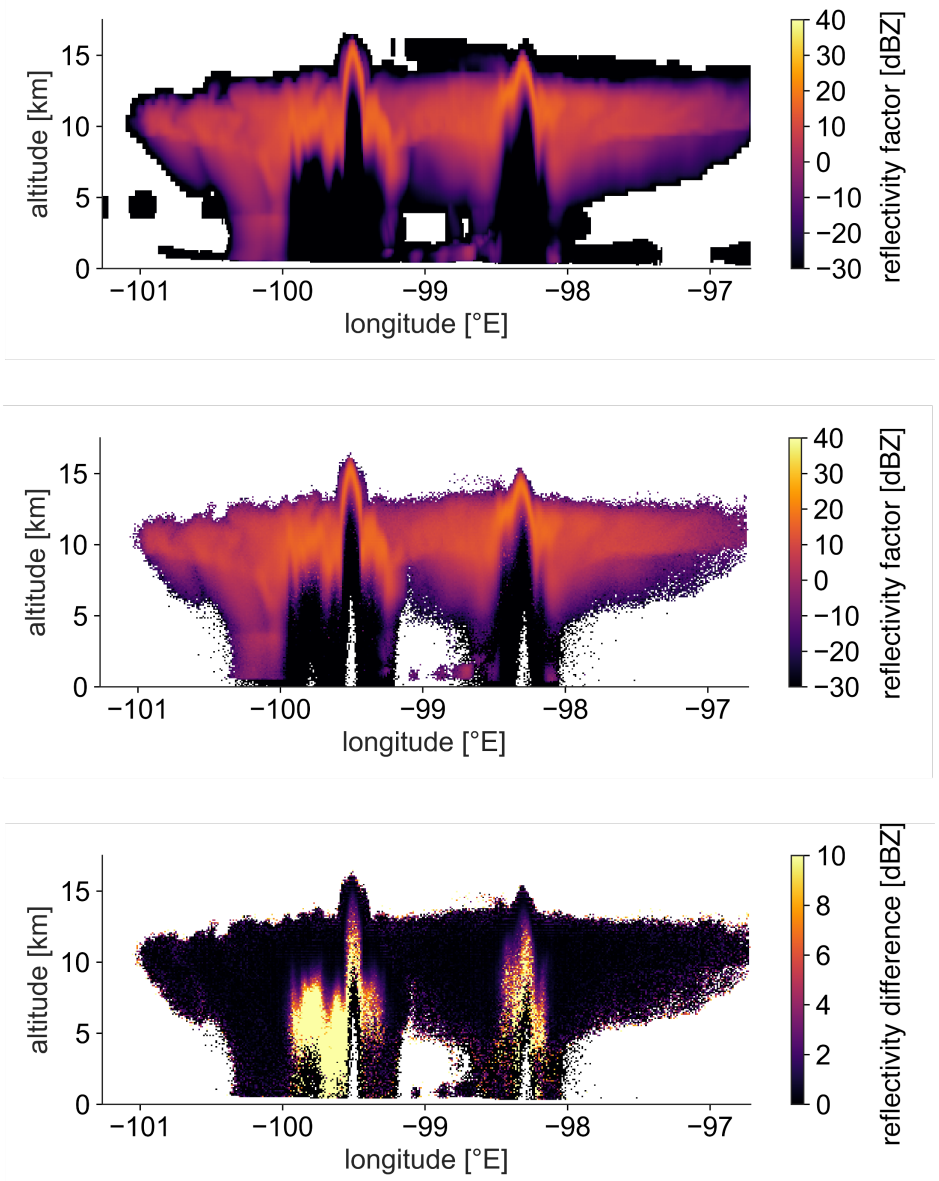

Figure 4: Top panel: W-band single scattering simulation of convective cells and associated anvil. Middle panel: Multiple scattering simulation of same cloud field as top. Bottom panel: Difference of middle and top showing the enhancement due to multiple scattering.

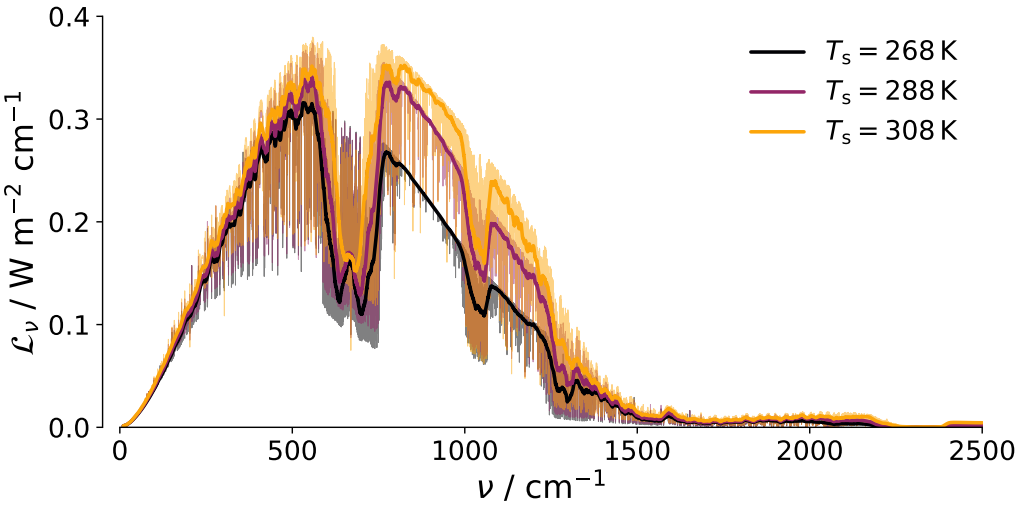

Figure 5: Simulated spectrally resolved outgoing longwave radiation $\mathcal{L}_\nu$ as a function of wavenumber ν for idealised atmospheres with different surface temperatures T_s. Shown are the spectra at a spectral resolution of 0.1 cm^{-1} (thin lines, perhaps invisible in printed version) and the 20 cm^{-1} moving averages (thick lines).

of those $\mathcal{L}_\nu$ spectra between 10 cm^{-1} and 2,500 cm^{-1} for surface temperatures of 268 K, 288 K, and 308 K, representing the spatial variations of Earth's surface temperature. Those simulations were then used to better understand the spectral longwave feedback derived from satellite observations.

Another very recent usage example of this capability is the study by He [138] that used ARTS for reference calculations of instantaneous 4xCO_2 forcing at different surface temperatures.

Spectral irradiance is calculated by integrating the normal component of spectral radiance over one hemisphere [139, Equation 2.53], where spectral radiance is the first element of the Stokes vector introduced in Equation 1. Integrating spectral irradiance over frequency then gives the total irradiance, that is, the total radiative energy flux in units of W/m^2. We define fluxes as a directed quantity in the context of 1D atmospheres, positive fluxes are directed upwards, negative fluxes are directed downwards, and the net flux is defined as the sum of the upward and downward flux.

ARTS has several ways to calculate radiation fluxes. For clear-sky fluxes there is an internal method, which uses the internal clear-sky radiative transfer solver to calculate spectral radiances. It assumes a plane parallel atmo-

spheres, for consistency with the all-sky solvers described below.

For all-sky fluxes, one can in principle use any of the discrete ordinate solvers available in ARTS, that is DISORT, RT4 and DOIT to calculate spectral radiances and then integrate them as mentioned above using internal integration methods. Due to the higher complexity when handling scattering, all-sky flux simulations are in general several times slower than clear-sky flux simulations. To mitigate this, we recommend to use DISORT as it is much faster than RT4 and DOIT and advanced features of the other solvers like polarization are of less interest for flux calculations. Furthermore, ARTS supports a dedicated DISORT mode for simulating fluxes, in which the integration over the hemisphere is done internally and very efficiently.

The flux simulation can be done with an arbitrary number of zenith angles over which the angular integration is done, and an arbitrary number of frequencies over which the spectral integration is done. As a rule of thumb, to get an accuracy in the order of $1\,\mathrm{W\,m^{-2}}$ for the fluxes, the number of zenith angles should be at least 6 and the number of frequencies should be in the order of several thousand. For reference calculations the number of frequencies should be even in the order of several ten thousand.

The left-hand columns of Figures 6 and 7 illustrate ARTS' capability of simulating long wave and short wave net fluxes for different atmospheric conditions. Figure 6 displays the results for a tropical atmosphere over the eastern Pacific with a thin liquid water cloud on top of the boundary layer and Figure 7 for a summer atmosphere over the North Atlantic with various cloud layers and types. Reference flux calculations for all-sky and clear-sky were done using ARTS-DISORT with 30,000 frequencies and 10 streams.

An interesting option for efficient flux calculations is that ARTS ships with a set of representative frequencies and associated quadrature weights derived by Paulina Czarnecki [140]. Stated very briefly, the idea is that a weighted mean over the spectral flux at these few frequencies gives an accurate estimate of the total flux. They are identified from high spectral resolution reference calculations for a diverse set of atmospheres by a combination of simulated annealing and linear regression, a method that was originally developed for efficiently simulating satellite observations [10]. In this case there are 64 representative frequencies each for longwave and shortwave. The calculations with this method are $30,000/64 \approx 470$ times faster than the reference calculations, results are marked with dots in Figures 6 and 7, illustrating the close agreement.

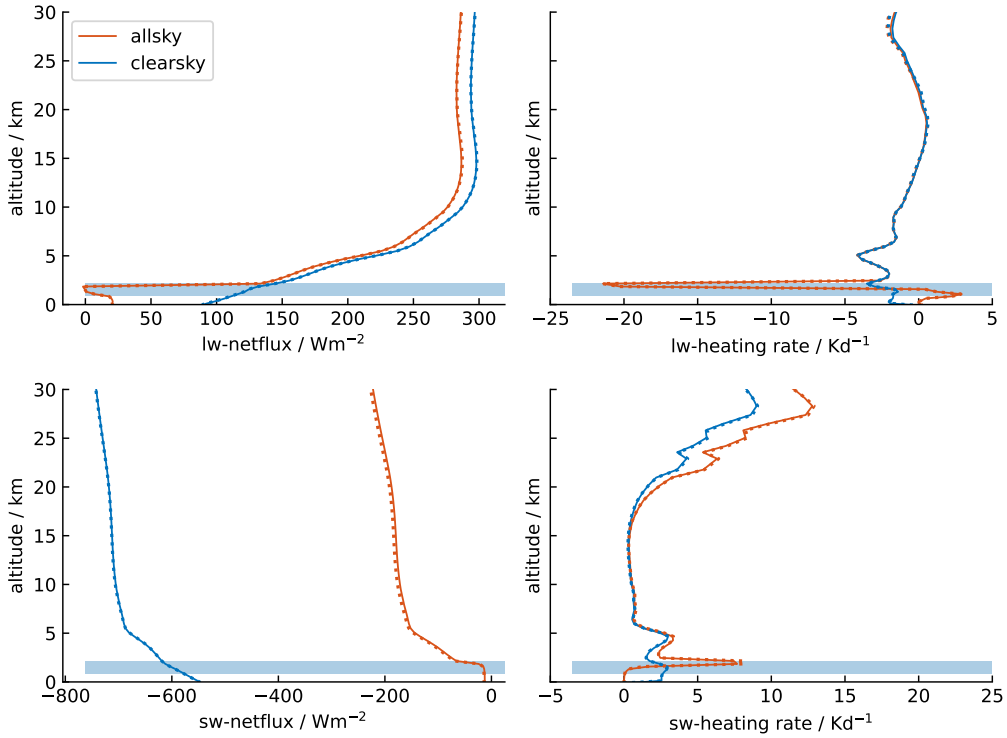

Figure 6: Simulation results for a modeled tropical atmosphere over the eastern Pacific with a thin but dense liquid water cloud on top of the boundary layer (peak liquid water content 0.4 g/m^3 at 1.3 km altitude, liquid water path 500 g/m^2). Solid lines show the reference setup and dots show the fast setup. The blue shaded area indicates the position of the liquid water cloud. Top left: All sky and clear sky long wave net flux. Bottom left: All sky and clear sky short wave net flux. A positive net flux denotes a net upward flux and a negative net flux a net downward flux. Top right: All sky and clear sky long wave heating rates. Bottom right: All sky and clear sky short wave heating rates.

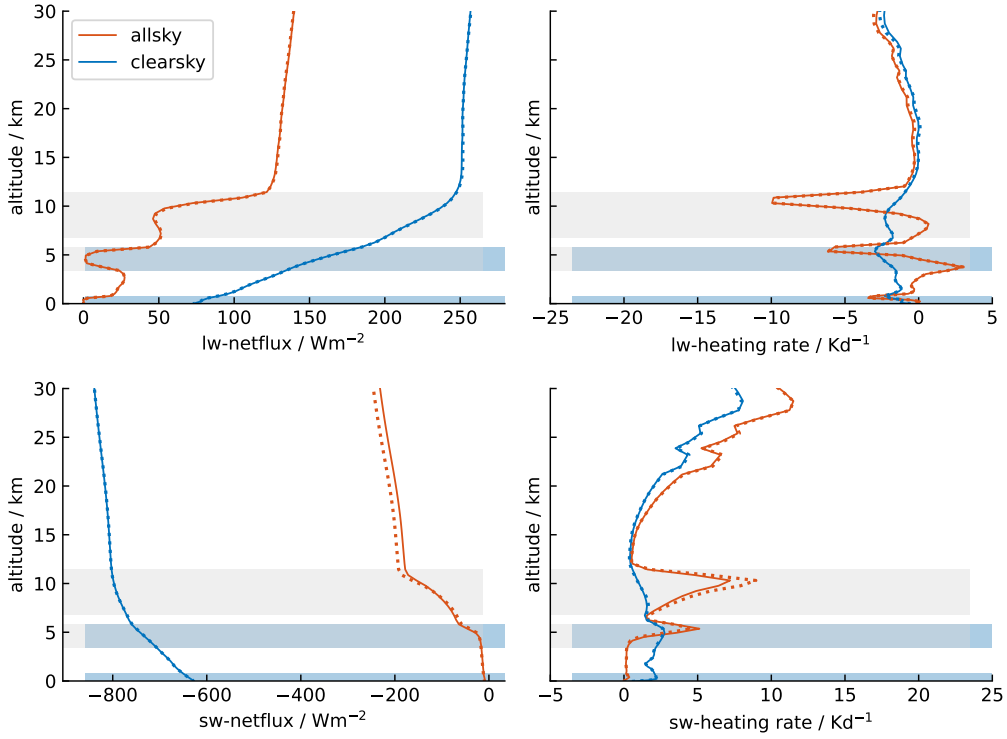

Figure 7: Simulation results for a modeled summer atmosphere over the North Atlantic. It contains a thin low level liquid water cloud, a mid level mixed phase cloud, and a high level ice cloud (total liquid water path 1450 g/m^2, frozen water path 93 g/m^2). Solid lines show the reference setup and dots show the fast setup. The blue shaded areas indicate the position of the liquid water clouds and the gray shaded areas the position of the frozen clouds. Top left: All sky and clear sky long wave net flux. Bottom left: All sky and clear sky short wave net flux. A positive net flux denotes a net upward flux and a negative net flux a net downward flux. Top right: All sky and clear sky long wave heating rates. Bottom right: All sky and clear sky short wave heating rates.

5.2. Heating rates

Based on the fluxes, ARTS also calculates radiative heating rates. Assuming hydrostatic equilibrium, the heating rate H is defined as

$$H = \frac{g}{c_p} \frac{dF_{net}}{dp}, \tag{29}$$

where g is the gravitational acceleration, c_p is the mass specific heat capacity at constant pressure and F_{net} is the net flux. The derivative is internally approximated with central differences and for the edges with a polynomial interpolation, which both are second order accurate. With this approximation, the heating rates are calculated on the same grid as the atmospheric state. The gravitational acceleration g depends on altitude and latitude and is calculated internally (formally the function takes also longitude as input, but this is currently not used). The specific heat capacity c_p theoretically depends on temperature (and for a non-ideal gas it could even depend on pressure) and has to be provided by the user. For practical purposes, the temperature and pressure dependence results from the temperature and pressure dependence of the atmospheric composition. But since c_p varies only weakly for typical atmospheric conditions on Earth, it can be approximately set to a constant. In the following example, c_p is set constant to the mass specific heat capacity of dry air $c_{p,air} = 1005.7\,\mathrm{J\,kg^{-1}K^{-1}}$ and g is varying with altitude.

The right columns of Figures 6 and 7 show the all-sky and clear-sky long wave (top) and short wave (bottom) heating rates for the selected example cases. In Figure 6 the liquid water cloud causes strong cooling in the long wave at the cloud top and weaker but also significant heating at the cloud bottom; in the short wave it causes some heating at the cloud top and suppresses the clear sky heating below. Dots again mark the fast approximation using the representative frequencies and weights. The very good agreement shows that the fast scheme is a very attractive option when spectral information is not needed. In Figure 7 the clouds cause strong cooling in the long wave at the cloud tops and weaker but also significant heating at the cloud bottoms except for the lowest cloud, where no heating occurs. In the short wave the clouds cause significant heating at the cloud tops in the middle and upper troposphere and suppress the clear sky heating below. At the lowest cloud the magnitude of sw-netflux is too small to create any significant amount of heating.

Note that the reason why the fast scheme works so well for heating rates is that heating rates were included as a training target, in addition to fluxes, in the derivation of the frequencies and weights [140]. This is necessary, because small fluctuations in the flux can have a large impact on its altitude gradient, the heating rate. This is particularly true at higher altitudes where the heat capacity is small due to low pressure.

Note also, though, that the training for the representative frequencies and weights was completely based on clear-sky simulations. It is therefore not completely self-understood that they would work equally well for all-sky simulations, as the figure seems to indicate, although we had hypothesized that this would be the case. The argument in favor of this is that clouds tend to make the radiation field more homogeneous across different frequencies, which makes the exact positions of the quadrature frequencies less critical. We have not yet done a proper quantitative evaluation of the accuracy of the fast scheme for all-sky simulations, but these first results seem promising.

Finally, it is worth mentioning that the representative frequencies and weights so far were only trained for present-day variations of water vapor, ozone, temperature and different CO_2 levels. There is work in progress on expanding that to variability in all greenhouse gases but for now the scheme will probably not work well for large perturbations in parameters not covered in the above list, for example for a significantly different methane concentration.

6. Optimal estimation retrievals

ARTS has supported retrievals since its first version by providing the Jacobian, but there has not been any built-in retrieval method. The standard alternative has been Qpack [4], providing a Matlab implementation of the optimal estimation method (OEM, [141]). OEM has now been integrated into ARTS, and, compared to [4], more efficient calculations and options can be offered.

6.1. Overview

The OEM is based on a Bayesian formulation of the inverse problem of finding an atmospheric state $\vec{x}$ consistent with a vector $\vec{y}$ of remote sensing observations using a forward model $F : \vec{x} \rightarrow \vec{y}_f$ that allows simulating observations corresponding to a given atmospheric state $\vec{x}$. The OEM is based on the assumptions that (1) the error affecting the observations is bias-free

Gaussian noise with covariance matrix $\mathbf{S}_e$ and that (2) a priori knowledge of the atmospheric state $\vec{x}$ can be described using a Gaussian distribution with a priori state $\vec{x}_a$ and a priori covariance matrix $\mathbf{S}_a$. By application of Bayes' theorem, the posterior distribution, which fully describes the solution of the inverse problem, is found to be [141, Equation 2.24]:

$$\begin{aligned} p(\vec{x}|\vec{y}) = \exp\Big(&- \frac{1}{2}(F(\vec{x}) - \vec{y})^T \mathbf{S}_e^{-1}(F(\vec{x}) - \vec{y}) \\ &- \frac{1}{2}(x - \vec{x}_a)^T \mathbf{S}_a^{-1}(\vec{x} - \vec{x}_a) \\ &+ \text{const.}\Big) \end{aligned} \tag{30}$$

If the underlying assumptions of the OEM hold true, the posterior distribution is Gaussian, too, and is fully specified by its mean and covariance matrix. The mean of the posterior distribution, which, due to the Gaussian nature of the posterior distribution, coincides with the maximum a posteriori estimator of $\vec{x}$, is typically found by minimizing the negative log-likelihood of (30), which is given by

$$\begin{aligned} -\log\left(p(\vec{x}|\vec{y})\right) = &\frac{1}{2}(F(\vec{x}) - \vec{y})^T \mathbf{S}_e^{-1}(F(\vec{x}) - \vec{y}) \\ &+ \frac{1}{2}(x - \vec{x}_a)^T \mathbf{S}_a^{-1}(\vec{x} - \vec{x}_a) \end{aligned} \tag{31}$$

Finding the posterior mean state of the inverse problem thus boils down to minimizing Equation 31. If the forward model F is linear, a global minimum of Equation 31 can be found in a single step using the Gauss-Newton method. However, for most applications in atmospheric remote sensing the forward model F is non-linear. In this case, Equation (31) has to be minimized iteratively. In addition to the Gauss-Newton (GN) method, the ARTS OEM method also provides an implementation of the Levenberg-Marquardt method (LM), which tends to be more stable for strongly non-linear forward models, such as those involving scattering.

Apart from the evaluation of the forward operator F, the computationally most complex operation in the application of the GN and LM optimizers is the solving of a linear system of equations, having a size following the number of elements in $\vec{x}$. Since solving such a linear system of equations explicitly may become prohibitively expensive in terms of computation time

and memory, all optimization methods in ARTS can be used with a conjugate gradient (CG) solver. The CG method solves the linear system iteratively and becomes computationally more efficient as the number of variables in $\vec{x}$ grows large.

6.2. ARTS integration

The ARTS OEM method aims to retain most of ARTS' flexibility in terms of performing forward simulations. To provide a maximum of flexibility in terms of foward model calculations, the OEM module interfaces with the rest of ARTS by an agenda. This agenda typically performs the following steps:

1. Unpack the vector $\vec{x}$ into the corresponding atmospheric fields and convert the elements to the forward model units,
2. perform the forward simulation,
3. apply required variable transformations to the Jacobian

Due to the flexibility of ARTS agendas this design allows most of ARTS' functionality to be used in a retrieval.

A principal benefit of the OEM integration into ARTS is that ARTS provides built-in functions that map elements of $\vec{x}$ to atmospheric fields and back. Moreover, retrieval grids may deviate from the forward model grids. Although the retrieval grid is not allowed to be broader than the corresponding forward model grid, it can cover a smaller range. Retrieved values are mapped to the forward model grids by using linear interpolation inside the ranges of the retrieval grids, and using nearest neighbour outside. That is, values at end points of retrieval grids are assumed to be valid all the way to end points of the forward model grids. ARTS also provides functionality to retrieve transformed variables and apply clipping, which helps avoid unphysical states that may lead to errors in the forward model calculation.

6.3. Handling of a priori and observation error covariance matrices

The calculations required to perform an OEM minimization step involve only the inverses of the covariance matrices $\mathbf{S}_a$ and $\mathbf{S}_e$. Since, depending on the retrieval problem at hand, the covariance matrices can grow relatively large, ARTS allows them to be provided either as $\mathbf{S}_a$ and $\mathbf{S}_e$ or directly as their inverses $\mathbf{S}_a^{-1}$ and $\mathbf{S}_e^{-1}$, respectively. In conjunction with the CG solver, this can drastically reduce memory requirements of the OEM calculation step and thus allow for the retrieval of a larger number of variables and observations simultaneously.

ARTS covariance matrices are represented as block-diagonal matrices, where each block can be provided either as normal covariance matrix or its inverse. Moreover, covariance matrix blocks can be dense or sparse matrices. This design supports the basic use case in which the user simply provides the covariance matrices but also allows for optimization of the memory footprint of the inversion by providing pre-computed and potentially sparse covariance matrices. The full covariance matrix can be represented as a single block, to allow full generalisation in the specification of correlations between variables.

7. Summary

This article gave an overview of the capabilities and limitations of ARTS version 2.6.

ARTS can compute atmospheric absorption by gases efficiently and accurately across the entire spectrum, from the radiowave to the UV/visible spectral range, including advanced features such as line mixing. Besides spectral line by spectral line absorption calculations, it also includes state of the art absorption continua, HITRAN collision-induced absorption, and a simple polynomial model fitted to HITRAN absorption cross-sections, which can be used for example for halocarbon species for which spectroscopic data are typically not available [20].

In the longwave spectral range, ARTS is established and well tested for both clear-sky and all-sky radiative transfer simulations. In the clear-sky case (without scattering) it uses its own native radiative transfer solver, which includes analytical Jacobians. It is fully polarized and includes advanced features such as an accurate treatment of Zeeman splitting.

For all-sky radiative transfer simulation, ARTS offers broad support to cover microwave scattering due to hydrometeors. Inside this domain, the main consideration for the future is to improve the calculation efficiency. It is today costly to make simulations with a high number of scattering elements, and one way forward is to allow specifying bulk scattering properties directly. A full re-implementation of the handling of scattering data is ongoing to open up for this development, as well as obtaining a more uniform code base around the different scattering solvers.

Based on the radiative transfer simulations, ARTS can also perform energy flux and heating rate calculations for both clear-sky and all-sky conditions. Furthermore, it has built-in methods for optimal-estimation-type retrievals of atmospheric state properties from remote observations.

Very recently, ARTS was extended to include a solar source term, so that it can simulate also clear-sky and all-sky shortwave radiative transfer simulations and based on that shortwave energy fluxes and heating rates. This new functionality is the subject of a separate article that is currently in preparation. Calculations with the shortwave part have so far considered molecular (Rayleigh) scattering and scattering by hydrometeors. Aerosol scattering (and absorption) could in principle be handled as well, but so far there are no ready-made databases of aerosol optical properties in the ARTS format.

Last but not least, it should be mentioned that ARTS is also used as a teaching tool in the international Master program Atmospheric Science at University of Hamburg (`https://www.mi.uni-hamburg.de/studium/20-atmo-science.html`) for courses on radiation and climate and on remote sensing.

Obtaining ARTS and contributing

The ARTS homepage, providing extensive documentation, is `https://radiativetransfer.org`. On GitHub, ARTS can be found at `https://github.com/atmtools/arts/releases`. For archiving purposes, there is also a package of the exact version described in this article on Zenodo [142].

The easiest way for Python users to obtain ARTS is through conda ('conda install -c rttools pyarts'). Pyarts is the python interface to ARTS, providing full ARTS functionality.

ARTS has been extensively tested and used on macOS, Linux, and other Unix systems. It has currently not been used or tested on Windows and there is also no conda package for Windows. This is planned to change for the next major version.

We welcome contributions. The for us most convenient way to contribute is through GitHub. Contributions can for example be bug fixes or extensions to the ARTS core, but also documentation, usage examples or helper tools.

Besides GitHub, a good way to communicate with other ARTS users and developers are the ARTS mailing lists (`https://www.radiativetransfer.org/contact`).

Acknowledgments

We are grateful to Aistė Schunck for cleaning up the references, and we thank the ARTS community, in particular Vasileios Barlakas, Oleksandr

Bobryshev, Jakob Dörr, Robin Ekelund, Gerrit Holl, gongxunhlj (Github handle), Lukas Kluft, Teresa Mendaza, Jana Mendrok, Jon Petersen, Marc Prange, Bengt Rydberg, Mayuri Tatiya and Takayoshi Yamada for contributing to the development of ARTS. We are also grateful to those that are active on the arts-users mailing list and help us respond to user questions.

For the Hamburg authors, this work is a contribution to the Centrum für Erdsystemforschung und Nachhaltigkeit (CEN). With its capabilities for calculating atmospheric energetics, ARTS also contributes to the Cluster of Excellence "CLICCS — Climate, Climatic Change, and Society". The work at Chalmers by PE and SP was supported by the Swedish National Space Agency (grants 65/18 and 166/18).

References

[1] T. Kuhn, A. Bauer, M. Godon, S. A. Buehler, K. Kuenzi, Water vapor continuum: Absorption measurements at 350 GHz and model calculations, J. Quant. Spectrosc. Radiat. Transfer 74 (5) (2002) 545–562. doi:10.1016/S0022-4073(01)00271-0.

[2] C. Emde, S. A. Buehler, C. Davis, P. Eriksson, T. R. Sreerekha, C. Teichmann, A polarized discrete ordinate scattering model for simulations of limb and nadir longwave measurements in 1D/3D spherical atmospheres, J. Geophys. Res. 109 (D24) (Dec. 2004). doi:10.1029/2004JD005140.

[3] T. R. Sreerekha, S. A. Buehler, C. Emde, A simple new radiative transfer model for simulating the effect of cirrus clouds in the microwave spectral region, J. Quant. Spectrosc. Radiat. Transfer 75 (2002) 611–624.

[4] P. Eriksson, C. Jiménez, S. A. Buehler, Qpack, a general tool for instrument simulation and retrieval work, J. Quant. Spectrosc. Radiat. Transfer 91 (1) (2005) 47–64. doi:10.1016/j.jqsrt.2004.05.050.

[5] S. A. Buehler, P. Eriksson, T. Kuhn, A. von Engeln, C. Verdes, ARTS, the atmospheric radiative transfer simulator, J. Quant. Spectrosc. Radiat. Transfer 91 (1) (2005) 65–93. doi:10.1016/j.jqsrt.2004.05.051.

[6] C. Davis, C. Emde, R. Harwood, A 3D polarized reversed Monte Carlo radiative transfer model for mm and sub-mm passive remote sensing in

cloudy atmospheres, IEEE T. Geosci. Remote 43 (5) (2005) 1096–1101. doi:10.1109/TGRS.2004.837505.

[7] C. Melsheimer, C. Verdes, S. A. Buehler, C. Emde, P. Eriksson, D. G. Feist, S. Ichizawa, V. O. John, Y. Kasai, G. Kopp, N. Koulev, T. Kuhn, O. Lemke, S. Ochiai, F. Schreier, T. R. Sreerekha, M. Suzuki, C. Takahashi, S. Tsujimaru, J. Urban, Intercomparison of general purpose clear sky atmospheric radiative transfer models for the millimeter/submillimeter spectral range, Radio Sci. 40 (2005). doi:10.1029/2004RS003110.

[8] S. A. Buehler, A. von Engeln, E. Brocard, V. O. John, T. Kuhn, P. Eriksson, Recent developments in the line-by-line modeling of outgoing longwave radiation, J. Quant. Spectrosc. Radiat. Transfer 98 (3) (2006) 446–457. doi:10.1016/j.jqsrt.2005.11.001.

[9] P. Eriksson, M. Ekström, C. Melsheimer, S. A. Buehler, Efficient forward modelling by matrix representation of sensor responses, Int. J. Remote Sensing 27 (9–10) (2007) 1793–1808. doi:10.1080/01431160500447254.

[10] S. A. Buehler, V. O. John, A. Kottayil, M. Milz, P. Eriksson, Efficient radiative transfer simulations for a broadband infrared radiometer — combining a weighted mean of representative frequencies approach with frequency selection by simulated annealing, J. Quant. Spectrosc. Radiat. Transfer 111 (4) (2010) 602–615. doi:10.1016/j.jqsrt.2009.10.018.

[11] S. A. Buehler, P. Eriksson, O. Lemke, Absorption lookup tables in the radiative transfer model ARTS, J. Quant. Spectrosc. Radiat. Transfer 112 (10) (2011) 1559–1567. doi:10.1016/j.jqsrt.2011.03.008.

[12] P. Eriksson, S. A. Buehler, C. P. Davis, C. Emde, O. Lemke, ARTS, the atmospheric radiative transfer simulator, version 2, J. Quant. Spectrosc. Radiat. Transfer 112 (10) (2011) 1551–1558. doi:10.1016/j.jqsrt.2011.03.001.

[13] R. Larsson, S. A. Buehler, P. Eriksson, J. Mendrok, A treatment of the Zeeman effect using Stokes formalism and its implementation in the Atmospheric Radiative Transfer Simulator (ARTS), J. Quant. Spectrosc. Radiat. Transfer 133 (2014) 445–453. doi:10.1016/j.jqsrt.2013.09.006.

[14] R. Larsson, A note on modelling of the oxygen spectral cross-section in the Atmospheric Radiative Transfer Simulator — Zeeman effect combined with line mixing in Earth's atmosphere, Int. J. Remote Sensing 35 (15) (2014) 5845–5853. doi:10.1080/01431161.2014.945002.

[15] R. Larsson, B. Lankhaar, P. Eriksson, Updated zeeman effect splitting coefficients for molecular oxygen in planetary applications, J. Quant. Spectrosc. Radiat. Transfer 224 (2019) 431–438. doi:10.1016/j.jqsrt.2018.12.004.

[16] R. Larsson, B. Lankhaar, Zeeman effect splitting coefficients for ClO, OH and NO in some earth atmosphere applications, J. Quant. Spectrosc. Radiat. Transfer 250 (2020) 107050. doi:10.1016/j.jqsrt.2020.107050.

[17] P. Eriksson, R. Ekelund, J. Mendrok, M. Brath, O. Lemke, S. A. Buehler, A general database of hydrometeor single scattering properties at microwave and sub-millimetre wavelengths, Earth Syst. Sci. Data 10 (3) (2018) 1301–1326. doi:10.5194/essd-10-1301-2018.

[18] M. Brath, R. Ekelund, P. Eriksson, O. Lemke, S. A. Buehler, Microwave and submillimeter wave scattering of oriented ice particles, Atmos. Meas. Tech. 13 (2020) 2309–2333. doi:10.5194/amt-13-2309-2020.

[19] R. V. Kochanov, I. E. Gordon, L. S. Rothman, K. P. Shine, S. W. Sharpe, T. J. Johnson, T. J. Wallington, J. J. Harrison, P. F. Bernath, M. Birk, G. Wagner, K. Le Bris, I. Bravo, C. Hill, Infrared absorption cross-sections in HITRAN2016 and beyond: Expansion for climate, environment, and atmospheric applications, J. Quant. Spectrosc. Radiat. Transfer 230 (2019) 172–221. doi:10.1016/j.jqsrt.2019.04.001.

[20] S. A. Buehler, M. Brath, O. Lemke, Ø. Hodnebrog, R. Pincus, P. Eriksson, I. Gordon, R. Larsson, A new halocarbon absorption model based on HITRAN cross-section data and new estimates of halocarbon instantaneous clear-sky radiative forcing, J. Adv. Model. Earth Syst. 14 (11) (2022). doi:10.1029/2022MS003239.

[21] S. A. Buehler, J. Mendrok, P. Eriksson, A. Perrin, R. Larsson, O. Lemke, ARTS, the atmospheric radiative transfer simulator — ver-

sion 2.2, the planetary toolbox edition, Geosci. Model Dev. 11 (4) (2018) 1537–1556. doi:10.5194/gmd-11-1537-2018.

[22] M. Mech, M. Maahn, S. Kneifel, D. Ori, E. Orlandi, P. Kollias, V. Schemann, S. Crewell, PAMTRA 1.0: the Passive and Active Microwave radiative TRAnsfer tool for simulating radiometer and radar measurements of the cloudy atmosphere, Geosci. Model Dev. 13 (9) (2020) 4229–4251. doi:10.5194/gmd-13-4229-2020.

[23] F. Schreier, S. G. Garcia, P. Hochstaffl, S. Staedt, Py4CAtSPYthon for Computational ATmospheric Spectroscopy, Atmosph. 10 (5) (2019). doi:10.3390/atmos10050262.

[24] I. Gordon, L. Rothman, R. Hargreaves, R. Hashemi, E. Karlovets, F. Skinner, E. Conway, C. Hill, R. Kochanov, Y. Tan, P. Wcisło, A. Finenko, K. Nelson, P. Bernath, M. Birk, V. Boudon, A. Campargue, K. Chance, A. Coustenis, B. Drouin, J. Flaud, R. Gamache, J. Hodges, D. Jacquemart, E. Mlawer, A. Nikitin, V. Perevalov, M. Rotger, J. Tennyson, G. Toon, H. Tran, V. Tyuterev, E. Adkins, A. Baker, A. Barbe, E. Canè, A. Császár, A. Dudaryonok, O. Egorov, A. Fleisher, H. Fleurbaey, A. Foltynowicz, T. Furtenbacher, J. Harrison, J. Hartmann, V. Horneman, X. Huang, T. Karman, J. Karns, S. Kassi, I. Kleiner, V. Kofman, F. Kwabia–Tchana, N. Lavrentieva, T. Lee, D. Long, A. Lukashevskaya, O. Lyulin, V. Makhnev, W. Matt, S. Massie, M. Melosso, S. Mikhailenko, D. Mondelain, H. Müller, O. Naumenko, A. Perrin, O. Polyansky, E. Raddaoui, P. Raston, Z. Reed, M. Rey, C. Richard, R. Tóbiás, I. Sadiek, D. Schwenke, E. Starikova, K. Sung, F. Tamassia, S. Tashkun, J. Vander Auwera, I. Vasilenko, A. Vigasin, G. Villanueva, B. Vispoel, G. Wagner, A. Yachmenev, S. Yurchenko, The hitran2020 molecular spectroscopic database, J. Quant. Spectrosc. Radiat. Transfer 277 (2022) 107949. doi:10.1016/j.jqsrt.2021.107949.

[25] P. Arendas, T. Furtenbacher, A. G. Csaszar, Selecting lines for spectroscopic (re)measurements to improve the accuracy of absolute energies of rovibronic quantum states, J. Cheminform. 13 (1) (2021). doi:10.1186/s13321-021-00534-y.

[26] W. Wang, A. Murk, E. Sauvageat, W. Fan, C. Daetwyler, M. Hervo, A. Haefele, K. Hocke, An indoor microwave radiometer for mea-

surement of tropospheric water, IEEE T. Geosci. Remote 61 (2023). doi:10.1109/TGRS.2023.3261067.

[27] F. Schranz, B. Tschanz, R. Ruefenacht, K. Hocke, M. Palm, N. Kaempfer, Investigation of Arctic middle-atmospheric dynamics using 3 years of H2O and O-3 measurements from microwave radiometers at Ny-Alesund, Atmos. Chem. Phys. 19 (15) (2019) 9927–9947. doi:10.5194/acp-19-9927-2019.

[28] M. Lainer, K. Hocke, N. Kampfer, Long-term observation of midlatitude quasi 2-day waves by a water vapor radiometer, Atmos. Chem. Phys. 18 (16) (2018) 12061–12074. doi:10.5194/acp-18-12061-2018.

[29] G. Mevi, G. Muscari, P. P. Bertagnolio, I. Fiorucci, G. Pace, VESPA-22: a ground-based microwave spectrometer for long-term measurements of polar stratospheric water vapor, Atmos. Meas. Tech. 11 (2) (2018) 1099–1117. doi:10.5194/amt-11-1099-2018.

[30] L. Pan, D. Lu, Terahertz band simulations using two different radiative transfer models, Sci. China-Earth Sci. 61 (10) (2018) 1482–1490. doi:10.1007/s11430-017-9242-3.

[31] E. Sauvageat, R. Albers, M. Kotiranta, K. Hocke, R. M. Gomez, G. Nedoluha, A. Murk, Comparison of Three High Resolution Real-Time Spectrometers for Microwave Ozone Profiling Instruments, IEEE J. Sel. Top. Appl. Rem. Sens. 14 (2021) 10045–10056. doi:10.1109/JSTARS.2021.3114446.

[32] F. Schranz, S. Fernandez, N. Kaempfer, M. Palm, Diurnal variation in middle- atmospheric ozone observed by ground- based microwave radiometry at Ny-Alesund over 1 year, Atmos. Chem. Phys. 18 (6) (2018) 4113–4130. doi:10.5194/acp-18-4113-2018.

[33] L. Bernet, T. von Clarmann, S. Godin-Beekmann, G. Ancellet, E. M. Barras, R. Stubi, W. Steinbrecht, N. Kampfer, K. Hocke, Ground-based ozone profiles over central Europe: incorporating anomalous observations into the analysis of stratospheric ozone trends, Atmos. Chem. Phys. 19 (7) (2019) 4289–4309. doi:10.5194/acp-19-4289-2019.

[34] D. A. Newnham, M. A. Clilverd, W. D. J. Clark, M. Kosch, P. T. Verronen, A. E. E. Rogers, Ground-based Ku-band microwave observations of ozone in the polar middle atmosphere, Atmos. Meas. Tech. 15 (8) (2022) 2361–2376. doi:10.5194/amt-15-2361-2022.

[35] L. Moreira, K. Hocke, N. Kaempfer, Short-term stratospheric ozone fluctuations observed by GROMOS microwave radiometer at Bern, Earth Planets Space 70 (2018). doi:10.1186/s40623-017-0774-4.

[36] N. J. Ryan, M. Palm, C. G. Hoffmann, J. Goliasch, J. Notholt, Ground-based millimetre-wave measurements of middle-atmospheric carbon monoxide above Ny-Alesund (78.9 degrees N, 11.9 degrees E), Atmos. Meas. Tech. 12 (7) (2019) 4077–4089. doi:10.5194/amt-12-4077-2019.

[37] Y. Shi, V. Shulga, O. Ivaniha, Y. Wang, O. Evtushevsky, G. Milinevsky, A. Klekociuk, A. Patoka, W. Han, D. Shulga, Comparison of Major Sudden Stratospheric Warming Impacts on the Mid-Latitude Mesosphere Based on Local Microwave Radiometer CO Observations in 2018 and 2019, Rem. Sens. 12 (23) (2020). doi:10.3390/rs12233950.

[38] Y. Wang, V. Shulga, G. Milinevsky, A. Patoka, O. Evtushevsky, A. Klekociuk, W. Han, A. Grytsai, D. Shulga, V. Myshenko, O. Antyufeyev, Winter 2018 major sudden stratospheric warming impact on midlatitude mesosphere from microwave radiometer measurements, Atmos. Chem. Phys. 19 (15) (2019) 10303–10317. doi:10.5194/acp-19-10303-2019.

[39] W. Krochin, F. Navas-Guzman, D. Kuhl, A. Murk, G. Stober, Continuous temperature soundings at the stratosphere and lower mesosphere with a ground-based radiometer considering the Zeeman effect, Atmos. Meas. Tech. 15 (7) (2022) 2231–2249. doi:10.5194/amt-15-2231-2022.

[40] J. Hagen, K. Hocke, G. Stober, S. Pfreundschuh, A. Murk, N. Kaempfer, First measurements of tides in the stratosphere and lower mesosphere by ground-based Doppler microwave wind radiometry, Atmos. Chem. Phys. 20 (4) (2020) 2367–2386. doi:10.5194/acp-20-2367-2020.

[41] J. Hagen, A. Murk, R. Rufenacht, S. Khaykin, A. Hauchecorne, N. Kampfer, WIRA-C: a compact 142-GHz-radiometer for continuous

middle-atmospheric wind measurements, Atmos. Meas. Tech. 11 (9) (2018) 5007–5024. doi:10.5194/amt-11-5007-2018.

[42] T. Lang, S. A. Buehler, M. Burgdorf, I. Hans, V. O. John, A new climate data record of upper-tropospheric humidity from microwave observations, Sci. Data 7 (218) (2020). doi:10.1038/s41597-020-0560-1.

[43] M. Prange, M. Brath, S. A. Buehler, Are elevated moist layers a blind spot for hyperspectral infrared sounders? – A model study, Atmos. Meas. Tech. 14 (11) (2021) 7025–7044. doi:10.5194/amt-14-7025-2021.

[44] J. He, H. Chen, Atmospheric Retrievals and Assessment for Microwave Observations from Chinese FY-3C Satellite during Hurricane Matthew, Rem. Sens. 11 (8) (2019). doi:10.3390/rs11080896.

[45] F. Schreier, M. Milz, S. A. Buehler, T. von Clarmann, Intercomparison of three microwave/infrared high resolution line-by-line radiative transfer codes, J. Quant. Spectrosc. Radiat. Transfer 211 (2018) 64–77. doi:10.1016/j.jqsrt.2018.02.032.

[46] O. Bobryshev, S. A. Buehler, V. O. John, M. Brath, H. Brogniez, Is there really a closure gap between 183.31 GHz satellite passive microwave and in-situ radiosonde water vapor measurements?, IEEE T. Geosci. Remote 56 (5) (2018) 2904–2910. doi:10.1109/TGRS.2017.2786548.

[47] I. Moradi, M. Goldberg, M. Brath, R. Ferraro, S. A. Buehler, R. Saunders, N. Sun, Performance of radiative transfer models in the microwave region, J. Geophys. Res.: Atm. 125 (6) (2020) e2019JD031831. doi:10.1029/2019JD031831.

[48] R. C. Scarlat, C. Melsheimer, G. Heygster, Retrieval of total water vapour in the Arctic using microwave humidity sounders, Atmos. Meas. Tech. 11 (4) (2018) 2067–2084. doi:10.5194/amt-11-2067-2018.

[49] W. He, Z. Wang, W. Wang, Z. Zhang, Sensitivity analysis of microwave spectrometer for atmospheric temperature and humidity sounding on the new generation fengyun satellite, IEEE J. Sel. Top. Appl. Rem. Sens. 16 (2023) 853–865. doi:10.1109/JSTARS.2022.3230845.

[50] P. E. Sheese, K. A. Walker, C. D. Boone, A. E. Bourassa, D. A. Degenstein, L. Froidevaux, C. T. McElroy, D. Murtagh, J. M. R. Iii, J. Zou, Assessment of the quality of ACE-FTS stratospheric ozone data, Atmos. Meas. Tech. 15 (5) (2022) 1233–1249. doi:10.5194/amt-15-1233-2022.

[51] H. Xu, H. Lu, Z. Wang, W. He, W. Wang, Effect Analysis of the Digital Spectrometer FFT Algorithm on THz Atmospheric Limb Sounder (TALIS) System Sensitivity, Rem. Sens. 13 (15) (2021). doi:10.3390/rs13152921.

[52] T. Yamada, T. O. Sato, T. Adachi, H. Winkler, K. Kuribayashi, R. Larsson, N. Yoshida, Y. Takahashi, M. Sato, A. B. Chen, R. R. Hsu, Y. Nakano, T. Fujinawa, S. Nara, Y. Uchiyama, Y. Kasai, HO2 Generation Above Sprite-Producing Thunderstorms Derived from Low-Noise SMILES Observation Spectra, Geophys. Res. Lett. 47 (3) (2020). doi:10.1029/2019GL085529.

[53] F. Grieco, K. Perot, D. Murtagh, P. Eriksson, B. Rydberg, M. Kiefer, M. Garcia-Comas, A. Lambert, K. A. Walker, Improvement of Odin/SMR water vapour and temperature measurements and validation of the obtained data sets, Atmos. Meas. Tech. 14 (8) (2021) 5823–5857. doi:10.5194/amt-14-5823-2021.

[54] W. Wang, Z. Wang, Y. Duan, Performance evaluation of THz Atmospheric Limb Sounder (TALIS) of China, Atmos. Meas. Tech. 13 (1) (2020) 13–38. doi:10.5194/amt-13-13-2020.

[55] Y. Duan, Z. Wang, H. Xu, W. Wang, Simulation of the Spectrum Response for the THz Atmosphere Limb Sounder (TALIS), Sensors 20 (2) (2020). doi:10.3390/s20020498.

[56] R. Song, M. Kaufmann, M. Ern, J. Ungermann, G. Liu, M. Riese, Three-dimensional tomographic reconstruction of atmospheric gravity waves in the mesosphere and lower thermosphere (MLT), Atmos. Meas. Tech. 11 (5) (2018) 3161–3175. doi:10.5194/amt-11-3161-2018.

[57] L. Li-cheng, G. Hai-yang, B. Ling-bing, Z. Qi-lin, W. Zhen, Inversion of Rotational Temperature in Airglow Layer Based on O-2 (0-1)

Atmospheric Band Spectrum, Spectrosc. Spectr. Anal. 40 (10) (2020) 3002–3009. doi:10.3964/j.issn.1000-0593(2020)10-3002-08.

[58] H. Gao, L. Li, L. Bu, Q. Zhang, Z. Wang, Y. Tang, Measurement of mesopause temperature using the mesospheric airglow spectrum photometer (MASP), Opt. Communic. 464 (2020). doi:10.1016/j.optcom.2020.125546.

[59] S. Pfreundschuh, P. Eriksson, D. Duncan, B. Rydberg, N. Hakansson, A. Thoss, A neural network approach to estimating a posteriori distributions of Bayesian retrieval problems, Atmos. Meas. Tech. 11 (8) (2018) 4627–4643. doi:10.5194/amt-11-4627-2018.

[60] I. S. Adams, S. J. Munchak, K.-S. Kuo, C. Pelissier, T. Clune, R. Kroodsma, A. Loftus, X. Li, Active and passive radiative transfer simulations for gmp-related field campaigns, in: 2019 IEEE International Geoscience and Remote Sensing Symposium (IGARSS 2019), IEEE International Symposium on Geoscience and Remote Sensing IGARSS, Inst Elect & Elect Engineers; Inst Elect & Elect Engineers, Geoscience & Remote Sensing Soc, 2019, pp. 4553–4556, iSSN: 2153-6996.

[61] V. Grützun, S. A. Buehler, L. Kluft, M. Brath, J. Mendrok, P. Eriksson, All-sky information content analysis for novel passive microwave instruments in the range from 23.8 GHz up to 874.4 GHz, Atmos. Meas. Tech. 11 (7) (2018) 4217–4237. doi:10.5194/amt-11-4217-2018.

[62] Y. Liu, G. G. Mace, Assessing synergistic radar and radiometer capability in retrieving ice cloud microphysics based on hybrid Bayesian algorithms, Atmos. Meas. Tech. 15 (4) (2022) 927–944. doi:10.5194/amt-15-927-2022.

[63] A. J. Geer, P. Bauer, K. Lonitz, V. Barlakas, P. Eriksson, J. Mendrok, A. Doherty, J. Hocking, P. Chambon, Bulk hydrometeor optical properties for microwave and sub-millimetre radiative transfer in RTTOV-SCATT v13.0, Geosci. Model Dev. 14 (12) (2021) 7497–7526. doi:10.5194/gmd-14-7497-2021.

[64] S. Li, L. Liu, H. Letu, S. Hu, P. Dong, H. Ren, J. Ye, Evaluation of the impacts of ice cloud vertical inhomogeneity on spaceborne pas-

sive submillimeter-wave simulations, Q. J. R. Meteorol. Soc. 149 (752) (2023) 1073–1089. doi:10.1002/qj.4457.

[65] F. Peers, P. Francis, S. J. Abel, P. A. Barrett, K. N. Bower, M. Cotterell, I, I. Crawford, N. W. Davies, C. Fox, S. Fox, J. M. Langridge, K. G. Meyer, S. E. Platnick, K. Szpek, J. M. Haywood, Observation of absorbing aerosols above clouds over the south-east Atlantic Ocean from the geostationary satellite SEVIRI - Part 2: Comparison with MODIS and aircraft measurements from the CLARIFY-2017 field campaign, Atmos. Chem. Phys. 21 (4) (2021) 3235–3254. doi:10.5194/acp-21-3235-2021.

[66] M. Brath, S. Fox, P. Eriksson, R. C. Harlow, M. Burgdorf, S. A. Buehler, Retrieval of an ice water path over the ocean from ISMAR and MARSS millimeter and submillimeter brightness temperatures, Atmos. Meas. Tech. 11 (2018) 611–632. doi:10.5194/amt-11-611-2018.

[67] K. D. Leppert, II, D. J. Cecil, Sensitivity of Simulated GMI Brightness Temperatures to Variations in Particle Size Distributions in a Severe Hailstorm, J. Appl. Meteorol. Clim. 58 (9) (2019) 1905–1930. doi:10.1175/JAMC-D-19-0031.1.

[68] S. Pfreundschuh, P. Eriksson, S. A. Buehler, M. Brath, D. Duncan, R. Larsson, R. Ekelund, Synergistic radar and radiometer retrievals of ice hydrometeors, Atmos. Meas. Tech. 13 (8) (2020) 4219–4245. doi:10.5194/amt-13-4219-2020.

[69] S. Pfreundschuh, S. Fox, P. Eriksson, D. Duncan, S. A. Buehler, M. Brath, R. Cotton, F. Ewald, Synergistic radar and sub-millimeter radiometer retrievals of ice hydrometeors in mid-latitude frontal cloud systems, Atmos. Meas. Tech. 15 (3) (2022) 677–699. doi:10.5194/amt-15-677-2022.

[70] Y. Liu, G. G. Mace, Synthesizing the Vertical Structure of Tropical Cirrus by Combining CloudSat Radar Reflectivity With In Situ Microphysical Measurements Using Bayesian Monte Carlo Integration, J. Geophys. Res.: Atm. 125 (18) (2020). doi:10.1029/2019JD031882.

[71] J. Gong, D. L. Wu, P. Eriksson, The first global 883 GHz cloud ice survey: IceCube Level 1 data calibration, processing and analysis, Earth

Syst. Sci. Data 13 (11) (2021) 5369–5387. doi:10.5194/essd-13-5369-2021.

[72] V. Barlakas, P. Eriksson, Three Dimensional Radiative Effects in Passive Millimeter/Sub-Millimeter All-sky Observations, Rem. Sens. 12 (3) (2020). doi:10.3390/rs12030531.

[73] F. Aires, C. Prigent, S. A. Buehler, P. Eriksson, M. Milz, S. Crewell, Towards more realistic hypotheses for the information content analysis of cloudy/precipitating situations - Application to a hyperspectral instrument in the microwave, Q. J. R. Meteorol. Soc. 145 (718, A) (2019) 1–14. doi:10.1002/qj.3315.

[74] R. Ekelund, P. Eriksson, S. Pfreundschuh, Using passive and active observations at microwave and sub-millimetre wavelengths to constrain ice particle models, Atmos. Meas. Tech. 13 (2) (2020) 501–520. doi:10.5194/amt-13-501-2020.

[75] V. Barlakas, V. S. Galligani, A. J. Geer, P. Eriksson, On the accuracy of RTTOV-SCATT for radiative transfer at all-sky microwave and submillimeter frequencies, J. Quant. Spectrosc. Radiat. Transfer 283 (2022) 108137. doi:10.1016/j.jqsrt.2022.108137.

[76] S. Fox, J. Mendrok, P. Eriksson, R. Ekelund, S. J. O'Shea, K. N. Bower, A. J. Baran, R. C. Harlow, J. C. Pickering, Airborne validation of radiative transfer modelling of ice clouds at millimetre and submillimetre wavelengths, Atmos. Meas. Tech. 12 (3) (2019) 1599–1617. doi:10.5194/amt-12-1599-2019.

[77] D. Casella, G. Panegrossi, P. Sano, B. Rydberg, V. Mattioli, C. Accadia, M. Papa, F. S. Marzano, M. Montopoli, Can We Use Atmospheric Targets for Geolocating Spaceborne Millimeter-Wave Ice Cloud Imager (ICI) Acquisitions?, IEEE T. Geosci. Remote 60 (2022). doi:10.1109/TGRS.2022.3145638.

[78] Y. Liu, S. A. Buehler, M. Brath, H. Liu, X. Dong, Ensemble optimization retrieval algorithm of hydrometeor profiles for the Ice Cloud Imager submillimeter-wave radiometer, J. Geophys. Res.: Atm. 123 (9) (2018) 4594–4612. doi:10.1002/2017JD027892.

[79] P. Eriksson, B. Rydberg, V. Mattioli, A. Thoss, C. Accadia, U. Klein, S. A. Buehler, Towards an operational Ice Cloud Imager (ICI) retrieval product, Atmos. Meas. Tech. 13 (2020) 53–71. doi:10.5194/amt-13-53-2020.

[80] V. S. Galligani, D. Wang, P. B. Corrales, C. Prigent, A Parameterization of the Cloud Scattering Polarization Signal Derived From GPM Observations for Microwave Fast Radative Transfer Models, IEEE T. Geosci. Remote 59 (11) (2021) 8968–8977. doi:10.1109/TGRS.2021.3049921.

[81] J. J. Coy, A. Bell, P. Yang, D. L. Wu, Sensitivity Analyses for the Retrievals of Ice Cloud Properties From Radiometric and Polarimetric Measurements in Sub-mm/mm and Infrared Bands, J. Geophys. Res.: Atm. 125 (13) (2020). doi:10.1029/2019JD031422.

[82] P. Dong, L. Liu, S. Li, S. Hu, L. Bu, Application of M5 Model Tree in Passive Remote Sensing of Thin Ice Cloud Microphysical Properties in Terahertz Region, Rem. Sens. 13 (13) (2021). doi:10.3390/rs13132569.

[83] C. Weng, L. Liu, T. Gao, S. Hu, S. Li, F. Dou, J. Shang, Multi-Channel Regression Inversion Method for Passive Remote Sensing of Ice Water Path in the Terahertz Band, Atmosph. 10 (8) (2019). doi:10.3390/atmos10080437.

[84] L. Liu, C. Weng, S. Li, L. Husi, S. Hu, P. Dong, Passive Remote Sensing of Ice Cloud Properties at Terahertz Wavelengths Based on Genetic Algorithm, Rem. Sens. 13 (4) (2021). doi:10.3390/rs13040735.

[85] L. Shu-Lei, L. Lei, G. Tai-Chang, S. Li-Huai, Q. Shi, H. Shuai, Radiation characteristics of the selected channels for cirrus remote sensing in terahertz waveband and the influence factors for the retrieval method, JIMW 37 (1) (2018) 60–71. doi:10.11972/j.issn.1001-9014.2018.01.012.

[86] H.-Y. Li, Z.-S. Wu, J.-J. Wu, L.-K. Lin, C.-S. Lu, Z.-W. Zhao, T. Qu, THz wave background radiation at upper troposphere, Multimed. Tools and Appl. 79 (13-14) (2020) 8767–8780. doi:10.1007/s11042-018-6803-x.

[87] F. Cutraro, V. S. Galligani, Y. Garcia Skabar, Evaluation of synthetic satellite images computed from radiative transfer models over a region

of South America using WRF and GOES-13/16 observations, Q. J. R. Meteorol. Soc. 147 (738) (2021) 2988–3003. doi:10.1002/qj.4111.

[88] R. Pincus, S. A. Buehler, M. Brath, C. Crevoisier, O. Jamil, K. F. Evans, J. Manners, R. L. Menzel, E. J. Mlawer, D. Paynter, R. L. Pernak, Y. Tellier, Benchmark calculations of radiative forcing by greenhouse gases, J. Geophys. Res.: Atm. 123 (23) (2020) e2020JD033483. doi:10.1029/2020JD033483.

[89] S. Bourdin, L. Kluft, B. Stevens, Dependence of Climate Sensitivity on the Given Distribution of Relative Humidity, Geophys. Res. Lett. 48 (8) (2021). doi:10.1029/2021GL092462.

[90] L. Kluft, S. Dacie, S. A. Buehler, H. Schmidt, B. Stevens, Re-examining the first climate models: Climate sensitivity of a modern radiative-convective equilibrium model, J. Climate 32 (23) (2019) 8111–8125. doi:10.1175/JCLI-D-18-0774.1.

[91] L. Kluft, S. Dacie, M. Brath, S. A. Buehler, B. Stevens, Temperature-dependence of the clear-sky feedback in radiative-convective equilibrium, Geophys. Res. Lett. 48 (22) (2021). doi:10.1029/2021GL094649.

[92] M. Gao, B. A. Franz, K. Knobelspiesse, P.-W. Zhai, V. Martins, S. Burton, B. Cairns, R. Ferrare, J. Gales, O. Hasekamp, Y. Hu, A. Ibrahim, B. McBride, A. Puthukkudy, P. J. Werdell, X. Xu, Efficient multi-angle polarimetric inversion of aerosols and ocean color powered by a deep neural network forward model, Atmos. Meas. Tech. 14 (6) (2021) 4083–4110. doi:10.5194/amt-14-4083-2021.

[93] C. Emde, H. Yu, A. Kylling, M. van Roozendael, K. Stebel, B. Veihelmann, B. Mayer, Impact of 3D cloud structures on the atmospheric trace gas products from UV-Vis sounders - Part 1: Synthetic dataset for validation of trace gas retrieval algorithms, Atmos. Meas. Tech. 15 (5) (2022) 1587–1608. doi:10.5194/amt-15-1587-2022.

[94] H. Yu, C. Emde, A. Kylling, B. Veihelmann, B. Mayer, K. Stebel, M. Van Roozendael, Impact of 3D cloud structures on the atmospheric trace gas products from UV-Vis sounders - Part 2: Impact on NO2 retrieval and mitigation strategies, Atmos. Meas. Tech. 15 (19) (2022) 5743–5768. doi:10.5194/amt-15-5743-2022.

[95] N. Mathew, S. Sahoo, R. R. Pillai, C. S. Raju, Millimeter-Wave Radiometric Information Content Analysis for Venus Atmospheric Constituents, Radio Sci. 55 (2) (2020). doi:10.1029/2019RS006913.

[96] R. Larsson, Y. Kasai, T. Kuroda, S. Sato, T. Yamada, H. Maezawa, Y. Hasegawa, T. Nishibori, S. Nakasuka, P. Hartogh, Mars submillimeter sensor on microsatellite: sensor feasibility study, Geosci. Instr., Methods and Data Syst. 7 (4) (2018) 331–341. doi:10.5194/gi-7-331-2018.

[97] D. I. Duncan, P. Eriksson, S. Pfreundschuh, An experimental 2D-Var retrieval using AMSR2, Atmos. Meas. Tech. 12 (12) (2019) 6341–6359. doi:10.5194/amt-12-6341-2019.

[98] D. Ciani, M. Sabatini, B. B. Nardelli, P. L. Dekker, B. Rommen, D. S. Wethey, C. Yang, G. L. Liberti, Sea surface temperature gradients estimation using top-of-atmosphere observations from the esa earth explorer 10 harmony mission: Preliminary studies, Rem. Sens. 15 (4) (2023). doi:10.3390/rs15041163.

[99] W. Jakob, J. Rhinelander, D. Moldovan, pybind11 – seamless operability between c++11 and python, https://github.com/pybind/pybind11 (2017).

[100] E. J. Mlawer, K. E. Cady-Pereira, J. Mascio, I. E. Gordon, The inclusion of the MT_CKD water vapor continuum model in the HITRAN molecular spectroscopic database, J. Quant. Spectrosc. Radiat. Transfer 306 (2023) 108645. doi:10.1016/j.jqsrt.2023.108645.

[101] K. P. Shine, I. V. Ptashnik, G. Rädel, The water vapour continuum: Brief history and recent developments, Sur. Geophy. 33 (2012) 535–555. doi:10.1007/s10712-011-9170-y.

[102] K. Schwarzschild, Ueber das gleichgewicht der sonnenatmosphäre, Nachrichten von der Gesellschaft der Wissenschaften zu Göttingen, Mathematisch-Physikalische Klasse 1906 (1) (1906) 41–53.

[103] P. Baron, S. Ochiai, E. Dupuy, R. Larsson, H. Liu, N. Manago, D. Murtagh, S. Oyama, H. Sagawa, A. Saito, T. Sakazaki, M. Shiotani, M. Suzuki, Potential for the measurement of mesosphere and

lower thermosphere (mlt) wind, temperature, density and geomagnetic field with superconducting submillimeter-wave limb-emission sounder 2 (smiles-2), Atmos. Meas. Tech. 13 (1) (2020) 219–237. doi:10.5194/amt-13-219-2020.

[104] C. Moler, C. Van Loan, Nineteen dubious ways to compute the exponential of a matrix, twenty-five years later, SIAM Review 45 (1) (2003) 3–49. doi:10.1137/S00361445024180.

[105] K. Stamnes, G. E. Thomas, J. J. Stamnes, Radiative Transfer in the Atmosphere and Ocean (2nd edition), Cambridge University Press, 2017, Ch. Chapter 3.3, p. 79. doi:10.1017/9781316148549.

[106] R. Buras, T. Dowling, C. Emde, New secondary-scattering correction in disort with increased efficiency for forward scattering, J. Quant. Spectrosc. Radiat. Transfer 112 (12) (2011) 2028–2034.

[107] D. Bates, Rayleigh scattering by air, Planetary and Space Science 32 (6) (1984) 785–790. doi:10.1016/0032-0633(84)90102-8.
URL http://www.sciencedirect.com/science/article/pii/0032063384901028

[108] J. E. Hansen, L. D. Travis, Light scattering in planetary atmospheres, Space Science Reviews 16 (4) (1974) 527–610. doi:10.1007/BF00168069.

[109] H. Tran, N. H. Ngo, J.-M. Hartmann, Efficient computation of some speed-dependent isolated line profiles, J. Quant. Spectrosc. Radiat. Transfer 129 (2013) 199–203. doi:10.1016/j.jqsrt.2013.06.015.

[110] R. R. Gamache, B. Vispoel, M. Rey, A. Nikitin, V. Tyuterev, O. Egorov, I. E. Gordon, V. Boudon, Total internal partition sums for the hitran2020 database, J. Quant. Spectrosc. Radiat. Transfer 271 (2021) 107713. doi:10.1016/j.jqsrt.2021.107713.

[111] M. R. Zaghloul, A. N. Ali, Algorithm 916: Computing the faddeyeva and voigt functions, ACM Trans. on Math. Softw. 38 (2) (2012). doi:10.1145/2049673.2049679.

[112] T. Yamada, L. Rezac, R. Larsson, P. Hartogh, N. Yoshida, Y. Kasai, Solving non-LTE problems in rotational transitions using the

Gauss-Seidel method and its implementation in the Atmospheric Radiative Transfer Simulator, A&A 619 (2018) A181. doi:10.1051/0004-6361/201833566.

[113] T. Karman, I. Gordon, A. van der Avoird, Y. I. Baranov, C. Boulet, B. J. Drouin, G. C. Groenenboom, M. Gustafsson, J.-M. Hartmann, R. L. Kurucz, L. S. Rothman, K. Sun, K. Sung, R. Thalman, H. Tran, E. H. Whishnow, R. Wordsworth, A. A. Vigasin, R. Volkamer, W. J. van der Zande, Update of the HITRAN collision-induced absorption section, Icarus (in press 2019). doi:10.1016/j.icarus.2019.02.034.

[114] M. I. Mishchenko, L. D. Travis, A. A. Lacis, Scattering, absorption, and emission of light by small particles, Cambridge University Press, 2002.

[115] G. W. Petty, W. Huang, The modified gamma size distribution applied to inhomogeneous and nonspherical particles: Key relationships and conversions, J. Atmos. Sci. 68 (7) (2011) 1460–1473.

[116] S. J. Abel, I. A. Boutle, An improved representation of the raindrop size distribution for single-moment microphysics schemes, Q. J. R. Meteorol. Soc. 138 (669) (2012) 2151–2162.

[117] J. Wang, X. Dong, B. Xi, A. J. Heymsfield, Investigation of liquid cloud microphysical properties of deep convective systems: 1. parameterization raindrop size distribution and its application for stratiform rain estimation, J. Geophys. Res.: Atm. 121 (18) (2016) 10–739.

[118] J. S. Marshall, W. M. Palmer, The distribution of raindrops with size, J. Meteorol. 5 (1948) 165–166, short Contribution. doi:10.1175/1520-0469(1948)005¡0165:TDORWS¿2.0.CO;2.

[119] G. M. McFarquhar, A. J. Heymsfield, Parameterization of tropical cirrus ice crystal size distributions and implications for radiative transfer: Results from cepex, J. Atmos. Sci. 54 (17) (1997) 2187–2200.

[120] P. R. Field, A. J. Heymsfield, A. Bansemer, Snow size distribution parameterization for midlatitude and tropical ice clouds, J. Atmos. Sci. 64 (12) (2007) 4346–4365.

[121] J. M. E. Delanoë, A. J. Heymsfield, A. Protat, A. Bansemer, R. J. Hogan, Normalized particle size distribution for remote sensing application, J. Geophys. Res.: Atm. 119 (7) (2014) 4204–4227.

[122] P. R. Field, A. J. Heymsfield, A. G. Detwiler, J. M. Wilkinson, Normalized hail particle size distributions from the t-28 storm-penetrating aircraft, J. Appl. Meteorol. Clim. 58 (2) (2019) 231–245.

[123] J. A. Milbrandt, M. K. Yau, A multimoment bulk microphysics parameterization. part i: Analysis of the role of the spectral shape parameter, J. Atmos. Sci. 62 (9) (2005) 3051–3064.

[124] I. S. Adams, J. Bobak, The Feasibility of Detecting Supercooled Liquid With a Forward-Looking Radiometer, IEEE J. Sel. Top. Appl. Rem. Sens. 11 (6, SI) (2018) 1932–1938, publisher: Institute of Elect & Electron Engineers Geoscience & Remote Sensing Soc; IEEE; IEEE GRSS. doi:10.1109/JSTARS.2018.2844684.

[125] C. F. Bohren, E. E. Clothiaux, Fundamentals of Atmospheric Radiation, WILEY-VCH Verlag GmbH & Co. KGaA, 2006, ISBN 3-527-40503-8.

[126] K. N. Liou, An Introduction to Atmospheric Radiation, 2nd Edition, Elsevier Science (USA), 2002, ISBN 0-12-451451-0.

[127] G. E. Thomas, K. Stamnes, Radiative Transfer in the Atmosphere and Ocean, Cambridge University Press, 1999, ISBN 0-521-89061-6.

[128] R. M. Goody, Y. L. Yung, Atmospheric Radiation: Theoretical Basis, 2nd Edition, Oxford University Press, 1989, ISBN 0-19-510291-6.

[129] I. Laszlo, K. Stamnes, W. J. Wiscombe, S.-C. Tsay, The discrete ordinate algorithm, disort for radiative transfer, in: A. Kokhanovsky (Ed.), Light Scattering Reviews, Volume 11: Light Scattering and Radiative Transfer, Springer Berlin Heidelberg, 2016, pp. 3–65. doi:10.1007/978-3-662-49538-4_1.

[130] K. F. Evans, G. L. Stephens, Microwave radiative transfer through clouds composed of realistically shaped ice crystals. part ii. remote sensing of ice clouds, J. Atmos. Sci. 52 (11) (1995) 2058–2072.

[131] S. Fox, An evaluation of radiative transfer simulations of cloudy scenes from a numerical weather prediction model at sub-millimetre frequencies using airborne observations, Rem. Sens. 12 (17) (2020). doi:10.3390/rs12172758.

[132] A. Battaglia, S. Tanelli, S. Kobayashi, D. Zrnic, R. J. Hogan, C. Simmer, Multiple-scattering in radar systems: A review, J. Quant. Spectrosc. Radiat. Transfer 111 (6) (2010) 917–947.

[133] T. Oguchi, N. Ishida, T. Ihara, Effect of multiple scattering on the estimation of rainfall rates using dual-wavelength radar techniques, IEEE T. Geosci. Remote 32 (4) (1994) 943–946. doi:10.1109/36.298023.

[134] A. Battaglia, M. O. Ajewole, C. Simmer, Multiple scattering effects due to hydrometeors on precipitation radar systems, Geophys. Res. Lett. 32 (19) (2005). doi:10.1029/2005GL023810.

[135] F. S. Marzano, L. Roberti, S. Di Michele, A. Mugnai, A. Tassa, Modeling of apparent radar reflectivity due to convective clouds at attenuating wavelengths, Radio Sci. 38 (1) (2003) 2–1–2–16. doi:10.1029/2002RS002613.

[136] F. E. Roemer, S. A. Buehler, M. Brath, L. Kluft, V. O. John, Direct observation of Earth's spectral long-wave feedback parameter, Nature Geosci. 16 (5) (2023) 416–421. doi:10.1038/s41561-023-01175-6.

[137] S. Dacie, L. Kluft, H. Schmidt, B. Stevens, S. A. Buehler, P. J. Nowack, S. Dietmüller, N. L. Abraham, T. Birner, A 1D RCE study of factors affecting the tropical tropopause layer and surface climate, J. Climate 32 (20) (2019) 6769–6782. doi:10.1175/JCLI-D-18-0778.1.

[138] H. He, R. J. Kramer, B. J. Soden, N. Jeevanjee, State dependence of CO_2 forcing and its implications for climate sensitivity, Nature 382 (6674) (2023) 1051–1056. doi:10.1126/science.abq6872.

[139] G. W. Petty, A First Course in Atmospheric Radiation, Sundog Publishing, 2004.

[140] P. Czarnecki, L. Polvani, R. Pincus, Sparse, empirically optimized quadrature for broadband spectral integration, Journal of Advances in Modeling Earth Systems 15 (10) (2023) e2023MS003819. doi:https://doi.org/10.1029/2023MS003819.

[141] C. D. Rodgers, Inverse methods for atmospheric sounding: theory and practice, Vol. 2, World scientific, 2000. doi:10.1142/3171.

[142] S. A. Buehler, P. Eriksson, O. Lemke, R. Larsson, S. Pfreundschuh, M. Brath, ARTS - The Atmospheric Radiative Transfer Simulator (2.6.6) (2024). doi:10.5281/zenodo.13326137.